A Repeating Fast Radio Burst Source in a Low-luminosity Dwarf Galaxy

Hewitt, D.M.; Bhardwaj, M.; Gordon, A.C.; Kirichenko, A.; Nimmo, K.; Bhandari, S.; Cognard, I.; Fong, W.-F.; de Paz, A.G.; Gopinath, A.; Hessels, J.W.T.; Kirsten, F.; Marcote, B.; Bezrukovs, V.; Blaauw, R.; Bray, J.D.; Buttaccio, S.; Cassanelli, T.; Chawla, P.; Corongiu, A.; Deng, W.; Didehbani, H.N.; Dong, Y.; Gawroński, M.P.; Giroletti, M.; Guillemot, L.; Huang, J.; Ivanov, D.V.; Joseph, R.C.; Kaspi, V.M.; Kharinov, M.A.; Lazda, M.; Lindqvist, M.; Maccaferri, G.; Mas-Ribas, L.; Masui, K.W.; Mckinven, R.; Melnikov, A.; Michilli, D.; Mikhailov, A.G.; Nugent, A.E.; Ould-Boukattine, O.S.; Paragi, Z.; Pearlman, A.B.; Pen, U.L.; Pleunis, Z.; Sand, K.R.; Shah, V.; Shin, K.; Snelders, M.P.; Venturi, T.; Wang, Na; Williams-Baldwin, D.R.A.; Yang, J.; Yuan, J.P.

DOI
10.3847/2041-8213/ad8ce1

Publication date
2024

Document Version
Final published version

Published in
Astrophysical Journal Letters

The Astrophysical Journal Letters, 977:L4 (17pp), 2024 December 10 https://doi.org/10.3847/2041-8213/ad8ce1

A Repeating Fast Radio Burst Source in a Low-luminosity Dwarf Galaxy

Danté M. Hewitt[1], Mohit Bhardwaj[2], Alexa C. Gordon[3], Aida Kirichenko[4], Kenzie Nimmo[5], Shivani Bhandari[1,6,7,8], Ismaël Cognard[9], Wen-fai Fong[3], Armando Gil de Paz[10,11], Akshatha Gopinath[1], Jason W. T. Hessels[1,6,12,13], Franz Kirsten[14], Benito Marcote[6,7], Vladislavs Bezrukovs[15], Richard Blaauw[6], Justin D. Bray[16], Salvatore Buttaccio[17,18], Tomas Cassanelli[19], Pragya Chawla[1,6], Alessandro Corongiu[17], William Deng[20,21], Hannah N. Didehbani[22], Yuxin Dong[3], Marcin P. Gawroński[23], Marcello Giroletti[18], Lucas Guillemot[9,24], Jeff Huang[12,13], Dmitriy V. Ivanov[25], Ronniy C. Joseph[12,13], Victoria M. Kaspi[12,13], Mikhail A. Kharinov[25], Mattias Lazda[20,26], Michael Lindqvist[14], Giuseppe Maccaferri[18], Lluis Mas-Ribas[27], Kiyoshi W. Masui[5,22], Ryan Mckinven[12,13], Alexey Melnikov[25], Daniele Michilli[5,22], Andrey G. Mikhailov[25], Anya E. Nugent[3], Omar S. Ould-Boukattine[1,6], Zsolt Paragi[7], Aaron B. Pearlman[12,13,30,31,32], Ue-Li Pen[26,28], Ziggy Pleunis[1,6], Ketan R. Sand[12,13], Vishwangi Shah[12,13], Kaitlyn Shin[5,22], Mark P. Snelders[1,6], Tiziana Venturi[18], Na Wang[29], David R. A. Williams-Baldwin[16], Jun Yang[29], and Jianping P. Yuan[29]

[1] Anton Pannekoek Institute for Astronomy, University of Amsterdam, Science Park 904, 1098 XH Amsterdam, The Netherlands; jason.hessels@mcgill.ca
[2] McWilliams Center for Cosmology, Department of Physics, Carnegie Mellon University, Pittsburgh, PA 15213, USA
[3] Center for Interdisciplinary Exploration and Research in Astrophysics (CIERA) and Department of Physics and Astronomy, Northwestern University, Evanston, IL 60208, USA
[4] Instituto de Astronomía, Universidad Nacional Autónoma de México, Apdo. Postal 877, Ensenada, Baja California 22800, Mexico
[5] MIT Kavli Institute for Astrophysics and Space Research, Massachusetts Institute of Technology, 77 Massachusetts Avenue, Cambridge, MA 02139, USA
[6] ASTRON, Netherlands Institute for Radio Astronomy, Oude Hoogeveensedijk 4, 7991 PD Dwingeloo, The Netherlands
[7] Joint Institute for VLBI ERIC, Oude Hoogeveensedijk 4, 7991 PD Dwingeloo, The Netherlands
[8] CSIRO Space and Astronomy, Australia Telescope National Facility, P.O. Box 76, Epping, NSW 1710, Australia
[9] Observatoire Radioastronomique de Nançay, Observatoire de Paris, Université PSL, Université d'Orléans, CNRS, 18330 Nançay, France
[10] Departamento de Física de la Tierra y Astrofísica, Facultad de CC. Físicas, Universidad Complutense de Madrid, E-28040, Madrid, Spain
[11] Instituto de Física de Partículas y del Cosmos IPARCOS, Facultad de CC. Físicas, Universidad Complutense de Madrid, E-28040 Madrid, Spain
[12] Trottier Space Institute, McGill University, 3550 rue University, Montréal, QC H3A 2A7, Canada
[13] Department of Physics, McGill University, 3600 rue University, Montréal, QC H3A 2T8, Canada
[14] Department of Space, Earth and Environment, Chalmers University of Technology, Onsala Space Observatory, 439 92, Onsala, Sweden
[15] Engineering Research Institute Ventspils International Radio Astronomy Centre (ERI VIRAC) of Ventspils University of Applied Sciences, Inzenieru street 101, Ventspils, LV-3601, Latvia
[16] Jodrell Bank Centre for Astrophysics, School of Physics and Astronomy, The University of Manchester, Alan Turing Building, Oxford Road, Manchester, M13 9PL, UK
[17] INAF-Osservatorio Astrofisico di Catania, via Santa Sofia 78, I-95123, Catania, Italy
[18] INAF-Istituto di Radioastronomia, Via Gobetti 101, 40129, Bologna, Italy
[19] Department of Electrical Engineering, Universidad de Chile, Av. Tupper 2007, Santiago 8370451, Chile
[20] University of Toronto, David Dunlap Institute for Astronomy and Astrophysics, St. George Street, Toronto, ON M5S 3H4, Canada
[21] University of Cambridge, Institute of Astronomy, Madingley Road, Cambridge CB3 0HA, UK
[22] Department of Physics, Massachusetts Institute of Technology, 77 Massachusetts Avenue, Cambridge, MA 02139, USA
[23] Institute of Astronomy, Faculty of Physics, Astronomy and Informatics, Nicolaus Copernicus University, Grudziadzka 5, PL-87-100 Toruń, Poland
[24] Laboratoire de Physique et Chimie de l'Environnement et de l'Espace, Université d'Orléans/CNRS, 45071 Orléans Cedex 02, France
[25] Institute of Applied Astronomy, Kutuzova Embankment 10, St. Petersburg, 191187, Russia
[26] David A. Dunlap Department of Astronomy & Astrophysics, University of Toronto, 50 St. George Street, Toronto, ON M5S 3H4, Canada
[27] University of California, Santa Cruz, UCO Observatories, 1156 High Street, Santa Cruz, CA 95064, USA
[28] Canadian Institute for Theoretical Astrophysics, University of Toronto, ON, Canada
[29] Xinjiang Astronomical Observatory, CAS, 150 Science 1-Street, Urumqi, Xinjiang 830011, People's Republic of China
Received 2024 September 5; revised 2024 October 22; accepted 2024 October 29; published 2024 November 29

Abstract

We present the localization and host galaxy of FRB 20190208A, a repeating source of fast radio bursts (FRBs) discovered using CHIME/FRB. As part of the Pinpointing REpeating ChIme Sources with EVN dishes repeater localization program on the European VLBI Network (EVN), we monitored FRB 20190208A for 65.6 hr at ∼1.4 GHz and detected a single burst, which led to its very long baseline interferometry localization with 260 mas uncertainty (2σ). Follow-up optical observations with the MMT Observatory ($i \gtrsim 25.7$ mag (AB)) found no visible host at the FRB position. Subsequent deeper observations with the Gran Telescopio Canarias, however, revealed an extremely faint galaxy ($r = 27.32 \pm 0.16$ mag), very likely (99.95%) associated with FRB 20190208A. Given the dispersion measure of the FRB (∼580 pc cm^{-3}), even the most conservative redshift estimate ($z_{\rm max} \sim 0.83$) implies

[30] Banting Fellow.
[31] McGill Space Institute Fellow.
[32] FRQNT Postdoctoral Fellow.

that this is the lowest-luminosity FRB host to date ($\lesssim 10^8\ L_\odot$), even less luminous than the dwarf host of FRB 20121102A. We investigate how localization precision and the depth of optical imaging affect host association and discuss the implications of such a low-luminosity dwarf galaxy. Unlike the other repeaters with low-luminosity hosts, FRB 20190208A has a modest Faraday rotation measure of a few tens of rad m^{-2}, and EVN plus Very Large Array observations reveal no associated compact persistent radio source. We also monitored FRB 20190208A for 40.4 hr over 2 yr as part of the Extragalactic Coherent Light from Astrophysical Transients repeating FRB monitoring campaign on the Nançay Radio Telescope and detected one burst. Our results demonstrate that, in some cases, the robust association of an FRB with a host galaxy will require both high localization precision and deep optical follow-up.

Unified Astronomy Thesaurus concepts: Radio bursts (1339); Radio transient sources (2008); Very long baseline interferometry (1769); Dwarf galaxies (416)

1. Introduction

Fast radio bursts (FRBs) are a class of extremely luminous, extragalactic, coherent radio transients that have durations on the order of milliseconds or less (for a review, see, e.g., E. Petroff et al. 2022). The majority of FRBs are observed as single events, but a small fraction (∼3%; CHIME/FRB Collaboration et al. 2023) are known to be repeaters (L. G. Spitler et al. 2016), from which multiple bursts have been detected. The repetition rate varies significantly among repeaters. While most repeaters have low repetition rates ($\sim 10^{-3}$–10^{-1} bursts hr^{-1} above a fluence threshold of 5 Jy ms), on par with the upper limits on the repetition rates of apparent nonrepeaters (CHIME/FRB Collaboration et al. 2023), some boast repetition rates about an order of magnitude larger, e.g., FRB 20201124A (A. E. Lanman et al. 2022) and FRB 20220912A (R. McKinven & CHIME/FRB Collaboration 2022). Broadband studies of a few active repeaters suggest that these rates are likely frequency-dependent (e.g., A. Josephy et al. 2019; P. Chawla et al. 2020), but most of the less active CHIME/FRB repeaters have not been well studied at higher frequencies.

The emission mechanism(s) and progenitor(s) of FRBs are not fully understood, but their short durations and high brightness temperatures ($\sim 10^{37}$ K) suggest neutron star or black hole origins, with magnetars being strong candidates in particular, given the energy demands of some high-repetition sources (e.g., B. D. Metzger et al. 2017). The magnetar hypothesis was further reinforced by the detection of an FRB-like burst from the Galactic magnetar SGR 1935+2154 (C. D. Bochenek et al. 2020; CHIME/FRB Collaboration et al. 2020).

Identifying the host galaxies of FRBs requires roughly arcsecond precision (or better) on the localization of the radio bursts (T. Eftekhari & E. Berger 2017). Studies of FRB hosts find that the majority are consistent with neutron star progenitors produced in core-collapse supernovae (CCSNe), but a small fraction are more consistent with progenitors from older stellar populations (A. C. Gordon et al. 2023; M. Bhardwaj et al. 2024; C. J. Law et al. 2024). While there is no clear statistical distinction between the hosts of repeaters and nonrepeaters (A. C. Gordon et al. 2023; M. Bhardwaj et al. 2024), tentatively, the hosts of repeaters do extend to lower masses, while nonrepeater hosts tend to be more optically luminous (K. E. Heintz et al. 2020; A. C. Gordon et al. 2023).

Of the 45 FRBs that have been associated with a host galaxy,[33] seven repeaters have been localized to milliarcsecond precision using the European VLBI Network (EVN), thus enabling characterization of the parsec-scale environment surrounding the source (B. Marcote et al. 2017, 2020; F. Kirsten et al. 2022; K. Nimmo et al. 2022b; S. Bhandari et al. 2023b; D. M. Hewitt et al. 2024; M. P. Snelders et al. 2024). Together with the challenges of acquiring very long baseline interferometry (VLBI) observations of sporadic transients, multiwavelength observations with matching resolution are required to leverage the astrometric precision achieved for the bursts themselves. These localizations revealed that some active repeaters are associated with star-forming regions —ideal birthplaces of magnetars formed via the core collapse of massive stars (J. S. Chittidi et al. 2021; Y. Dong et al. 2024) —while some are slightly offset from local peaks of star formation (C. G. Bassa et al. 2017; S. P. Tendulkar et al. 2021). One repeater even inhabits a globular cluster (F. Kirsten et al. 2022), necessitating delayed magnetar formation channels, such as binary neutron star merger or accretion-induced collapse of a white dwarf, for at least some sources (K. Kremer et al. 2021).

The focus of this present work is on FRB 20190208A, a repeater discovered by CHIME/FRB (E. Fonseca et al. 2020). To date, CHIME/FRB has detected 15 bursts in total from this source,[34] including seven baseband events (with raw-voltage data recorded) between 2020 January and 2021 December (R. Mckinven et al. 2023). The bursts show high fractions of linear polarization and some tentative evidence of minor fluctuations in the polarization position angle (PPA) toward the edges of the bursts. The reported dispersion measure (DM) has been stable around 580 pc cm^{-3} across 2020 and 2021, while the observed Faraday rotation measure (RM) has shown "u-shaped" evolution over this same period, decreasing from ∼30 to ∼10 rad m^{-2}, before increasing again to ∼30 rad m^{-2}. To our knowledge, there are no other detections of FRB 20190208A in the literature.

In this paper, we present a VLBI localization of FRB 20190208A using the EVN. Leveraging this precise localization, we performed optical follow-up observations to identify the host galaxy and searched for any associated compact persistent radio emission. We also present the results of two targeted radio monitoring campaigns at ∼1.4 GHz, which totaled more than 100 hr of exposure and resulted in two bursts being detected from FRB 20190208A. These are the first bursts that have been observed from this source by a telescope other than CHIME/FRB. Section 2 describes the various radio observations, the source localization, and the properties of the detected bursts. Section 3 describes the subsequent optical observations and host galaxy association. In Section 4, we discuss our results. Detailed descriptions of pipelines,

[33] The FRB Community Newsletter (Volume 05, Issue 07, DOI:10.7298/PRE0-VF51).

[34] www.chime-frb.ca/repeaters/FRB20190208A

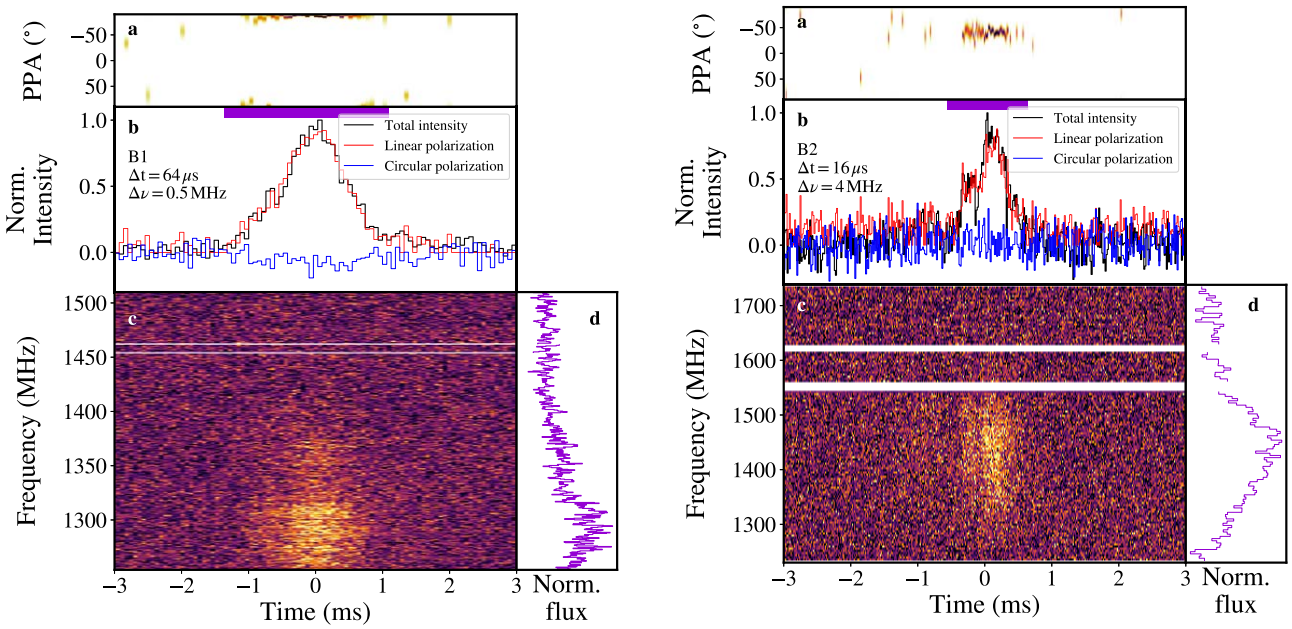

Figure 1. The left and right panels show bursts B1 and B2, detected in the PRECISE and ÉCLAT projects, respectively. In each subfigure, a dynamic spectrum of the burst is shown in panel (c). Bursts B1 and B2 have been dedispersed using DMs of 580.1 and 579.9 pc cm^{-3}, respectively. The horizontal white lines indicate channels contaminated by RFI that have been masked. A frequency-averaged (over the entire observing band) total intensity profile of the burst is shown in black in panel (b). The unbiased linear polarization is shown in red and the circular polarization in blue. In panel (a), the probability density function of the PPA, at each time step, is shown. The bursts have been derotated according to their respective RMs (46.5 rad m^{-2} for B1 and −5.2 rad m^{-2} for B2), and the PPA is referenced to infinite frequency. In panel (d), the time-averaged frequency spectrum (integrated over the burst duration indicated by the horizontal purple bar in panel (b)) is shown in purple. Note that the observing bandwidths differ between the two instruments.

observation logs, and analyses of the bursts are presented in Appendices A–C. Throughout this work, we assume Planck18 cosmological parameters (Planck Collaboration et al. 2020).

2. Radio Observations and Interferometric Localization

2.1. EVN Observations

We observed the FRB 20190208A field 38 times between 2021 February and 2023 August using an ad hoc array of EVN dishes, in "EVN-Lite" mode,[35] at a central frequency of ∼1.4 GHz. The total exposure time on FRB 20190208A, accounting for phase-referencing scans of a nearby calibrator, was 65.6 hr. These observations were carried out as part of the ongoing FRB VLBI localization campaign called Pinpointing REpeating ChIme Sources with EVN dishes (PRECISE; PI: F. Kirsten; see, e.g., B. Marcote et al. 2022). We detected a single burst (which we will refer to as B1) in one observation, described below. The other observations had a similar setup in terms of calibrator source selection, observing strategy, and recording details, but the array configuration somewhat differed depending on the availability of dishes. In all observations, the 100 m Effelsberg telescope participated, and these single-dish data were searched for bursts.

We detected B1 (left panel in Figure 1) in an observation on 2021 October 17, lasting from 08:49 UT to 11:23 UT (PRECISE project code PR187A), using nine EVN dishes: Badary, Effelsberg, Irbene, Medicina, Onsala, Svetloe, Toruń, Urumqi, and Zelenchukskaya. Detailed descriptions of the observational setup and search pipeline are presented in Appendix A.

We observed a test pulsar, PSR B2255+58, for 5 minutes at the beginning and end of the observation to assess data quality and verify the polarimetric calibration. After the first test pulsar scan, we observed J1419+5423 for 5 minutes to use as a fringe finder and bandpass calibrator. For phase referencing, we alternated between 1.5 minute scans of our chosen phase calibrator, J1852+4855 (2.°0 offset from the preliminary FRB 20190208A position[36]), and 5.5 minute scans of FRB 20190208A. Finally, we also observed the source J1850+4959 (1.°1 offset from the phase calibrator) as an interferometric check source (see Section 2.5 and Appendix A). The total exposure time on FRB 20190208A during this one session with a detected burst was ∼97 minutes.

2.2. Nançay Radio Telescope Observations

The Extragalactic Coherent Light from Astrophysical Transients (ÉCLAT; PI: D. Hewitt) observing campaign on the Nançay Radio Telescope (NRT) has been performing targeted follow-up observations of repeating FRBs since the start of 2022. About 20 CHIME/FRB repeaters are observed for approximately 1 hr week^{-1} each. Observations are conducted at a central frequency of 1.484 GHz using the low-frequency receiver (1.1–1.8 GHz) of the focal plane and receiver system, Foyer Optimisé pour le Radio Télescope. The Nançay Ultimate Pulsar Processing Instrument (NUPPI; G. Desvignes et al. 2011) records full-polarization data (on a linear basis) with 32 bit sampling, 16 μs time resolution, and a total observing bandwidth of 512 MHz—consisting of eight 64 MHz subbands divided into 4 MHz channels. We applied coherent dedispersion (i.e., dedispersion *within* spectral

[35] EVN-Lite is a new initiative to address rare/transient phenomena requiring hundreds of hours of observing time with ad hoc subarrays of radio telescopes that form the EVN, outside the regular EVN observing sessions.

[36] An arcminute-level position for FRB 20190208A was made available through a Memorandum of Understanding between the PRECISE project and the CHIME/FRB Collaboration.

channels) at a DM of 579 pc cm^{-3} for FRB 20190208A.[37] Additionally, a 10 s observation of a 3.33 Hz pulsed noise diode is also acquired with each ÉCLAT FRB observation for polarimetric calibration.

Between 2022 February and 2023 December, FRB 20190208A was observed 52 times, resulting in a total exposure time of 40.4 hr. The search pipeline is summarized in Appendix B. We detected a single FRB 20190208A burst in our ÉCLAT observations on 2023 May 17, which we will refer to as B2 (right panel in Figure 1).

2.3. Very Large Array Observations

We searched for persistent radio continuum emission in the field of FRB 20190208A using the Karl G. Jansky Very Large Array (VLA) in the C configuration. Observations were conducted on 2021 October 19 23:36:00 UT as part of program VLA/22B-126 (PI: S. Bhandari) in the 4–8 GHz *C* band, divided into 32 × 128 MHz spectral windows and centered at a frequency of 6 GHz. Sources 3C 286 and J1852+4855 were used as flux and phase calibrators, respectively. The target field was observed for 71.6 minutes, yielding an rms noise of 4 μJy beam^{-1}, but no persistent radio source (PRS) was detected at the position of FRB 20190208A. We used the VLA pipeline calibration and performed imaging, with Briggs's weighting (robust = 0.5) and a cell size of 1″, in `CASA` (J. P. McMullin et al. 2007; I. M. van Bemmel et al. 2022) using the task `tclean`. The resulting synthesized beam size was 3.″2 × 2.″8.

2.4. Properties of the Bursts

The properties of bursts B1 and B2 are summarized in Table 1. In this section, we briefly summarize these properties, while detailed descriptions of the analyses are presented in Appendix C.

We estimate the DM of B1 and B2 to be 580.1 and 579.9 pc cm^{-3}, respectively, which is consistent with previous estimates by CHIME/FRB (E. Fonseca et al. 2020; R. Mckinven et al. 2023). The estimated DM contribution from the Milky Way thin/thick-disk interstellar medium is 71.5 pc cm^{-3} (using NE2001p; S. K. Ocker & J. M. Cordes 2024). The expected scattering timescales from the Milky Way at the center frequencies of the PRECISE and ÉCLAT observing bands are 0.137 and 0.103 μs, respectively, significantly smaller than the time resolution of our data. The lack of substantial scattering is also visible in the burst profiles (Figure 1) and bodes well for probing the bursts for microstructure. To do so, we produced filter-bank data for B1 at time resolutions of 64, 16, and 4 μs but find no prominent structure on these timescales. We find RMs of $+46.5 \pm 16.5$ and -5.2 ± 4.9 rad m^{-2} for B1 and B2, respectively. These values have not been corrected for the Galactic RM contribution for this line of sight ($+4 \pm 12$ rad m^{-2}; S. Hutschenreuter et al. 2022) or the expected ionospheric contributions of 1.07 ± 0.07 and 1.39 ± 0.09 rad m^{-2} for B1 and B2, respectively. Taking uncertainties into account, the RM for B1 is consistent with RM$_{QU} = 25.75 \pm 18$ rad m^{-2} measured for a CHIME/FRB FRB 20190208A burst detected 8 days earlier (R. Mckinven et al. 2023). All together, these burst properties and propagation effects indicate a relatively clean line of sight toward the source.

[37] This is the rounded DM of the most recent FRB 20190208A burst detected by CHIME/FRB at the start of ÉCLAT monitoring.

Table 1
Properties of the Bursts Detected from FRB 20190208A at 1.4 GHz

Property	B1	B2
Telescope	EVN	NRT
TOA[a]	59504.40346933	60081.13824472
Burst width[b] (ms)	1.13 ± 0.03	0.65 ± 0.03
Fluence[c] (Jy ms)	1.70 ± 0.34	0.95 ± 0.19
Bandwidth[d] (MHz)	$>97 \pm 5$	191 ± 8
DM$_{S/N}$[e] (pc cm^{-3})	580.01 ± 0.26	580.03 ± 0.14
DM$_{struct}$[f] (pc cm^{-3})	580.24 ± 0.23	579.84 ± 0.29
RM$_{obs}$[g] (rad m^{-2})	$+46.5 \pm 16.5$	-5.2 ± 4.9
RM$_{iono}$[h] (rad m^{-2})	1.07 ± 0.07	1.39 ± 0.09

Notes.
[a] The burst time of arrival at the solar system barycenter in TDB, corrected to infinite frequency for a DM of 580 pc cm^{-3} and using a DM constant of $1/(2.41 \times 10^{-4})$ MHz^2 pc^{-1} cm^3 s. Measured at the time bin corresponding to the peak flux density. The position for Effelsberg is $X = 4033947.2355$ m, $Y = 486990.7943$ m, $Z = 4900431.0017$ m, and for the NRT, $X = 4324165.81$ m, $Y = 165927.11$ m, $Z = 4670132.83$ m.
[b] FWHM of a Gaussian fit to the frequency-averaged profile.
[c] We assume an uncertainty of approximately 20%, dominated by the uncertainty on the system equivalent flux density.
[d] FWHM of a Gaussian fit to the time-averaged spectrum.
[e] DM determined from S/N optimization (see Appendix C.1).
[f] DM determined from structure optimization using `DM_phase` (A. Seymour et al. 2019; see Appendix C.1).
[g] See Appendices C.3 and C.4. We caution that there is a sign ambiguity.
[h] The expected ionospheric RM contributions using IonFR (C. Sotomayor-Beltran et al. 2013).

FRB 20190208A appears to be more active at CHIME/FRB frequencies than at ∼1.4 GHz. To quantify the frequency-dependent activity, we calculate the statistical spectral index, which compares the rates at two different frequencies, taking into account instrumental sensitivity. We find values of $\alpha_{s,NRT/CHIME} = -2.30 \pm 0.46$ and $\alpha_{s,EFF/CHIME} = -2.96 \pm 0.49$. Within the errors, these values are more or less comparable to what has been measured for other repeaters like FRB 20121102A (L. J. M. Houben et al. 2019) and FRB 20180916B (P. Chawla et al. 2020). Notably, all these sources appear to be less active at higher frequencies.

2.5. EVN Correlation and Localization

A detailed description of correlation passes, the step-by-step localization procedure, and the FRB positional uncertainty estimation is presented in Appendix A.

The PRECISE data underwent multiple correlation iterations at the Joint Institute for VLBI ERIC (JIVE) in the Netherlands (EVN correlation proposal EK050; PI: F. Kirsten) using the software correlator `SFXC` (A. Keimpema et al. 2015).

We calibrated and imaged the EVN data using standard interferometric techniques in `AIPS` (E. W. Greisen 2003) and `DIFMAP` (M. C. Shepherd et al. 1994). Calibration solutions were derived from the fringe finder (J1419+5423) and phase calibrator (J1852+4855, with a positional uncertainty of $\Delta\alpha = 0.15$ mas, $\Delta\delta = 0.10$ mas from the RFC 2023B catalog[38]) before being applied to the interferometric check source (J1850+4959) to verify that the calibration was successful and to help assess the precision of our localization. Using `DIFMAP`, with a natural weighting scheme and cell size of 1 mas (in each

[38] astrogeo.org/sol/rfc/rfc_2023b/rfc_2023b_cat.html

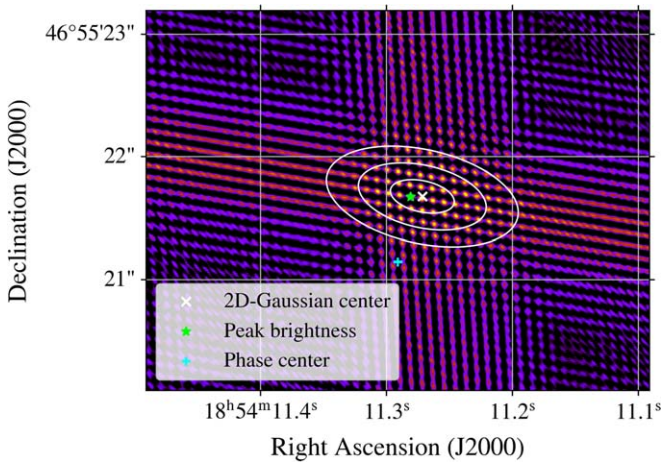

Figure 2. Dirty map of B1, the burst from FRB 20190208A detected in PRECISE observations. The cyan plus sign indicates the position of the phase center, the green star shows the position of the pixel with the peak brightness, and the white cross marks the center of the Gaussian ellipse.

dimension), we imaged the check source and measured its position. Compared to its position in the RFC 2023B catalog (which has an uncertainty of $\Delta\alpha = 0.20$ mas, $\Delta\delta = 0.15$ mas), we found a positional offset of $\Delta\alpha = 1.46$ mas, $\Delta\delta = 0.03$ mas. Given our synthesized beam size of 54×23 mas, we thus conclude that our calibration was successful. The calibration solutions were then applied to the target field of FRB 20190208A before imaging (again using `DIFMAP` with natural weighting and a cell size of 1 mas).

Unfortunately, the spectral extent of B1 was covered by the observing bands of only three dishes: Effelsberg, Onsala, and Toruń (Figure 7). Fortunately, however, the two baselines given by these dishes are oriented nearly orthogonal with respect to each other, and so the fringe pattern forms a cross-like shape, shown in Figure 2. Although the subarcsecond position of FRB 20190208A is clear from this map, the relatively poor *uv*-coverage results in less precise localization compared to previous EVN VLBI localizations of repeaters, though still on par with what is expected from localizations of individual bursts (see, e.g., K. Nimmo et al. 2022b; D. M. Hewitt et al. 2024).

In the case of FRB 20190208A presented here, there are multiple side lobes of comparable brightness, where the fringes from the baselines intersect. Providing a statistical confidence region for the FRB position is thus nontrivial. To quantify the localization region, we fit a 2D Gaussian function to all pixels where the absolute value of the dirty map of the burst is above 3σ. This 2D Gaussian fit has $\sigma_x = 127$ mas, $\sigma_y = 265$ mas, and $\theta = 0.217$ rad (measured clockwise in the dirty map presented in Figure 2). The ellipses shown in Figure 2 are the 1σ, 2σ, and 3σ contours of this Gaussian fit. These are not traditional confidence error ellipses; rather, these ellipses contain 68.3%, 95.4%, and 99.7% of the map pixels with power above 3σ. The center position of this 2D Gaussian (the white cross in the map) is located near the nominal peak brightness position (the green star).

The position we find for FRB 20190208A, with conservative uncertainty estimates from the 2-σ_y contour of the 2D Gaussian fit, is

R.A. (J2000) $= 18^{\rm h}54^{\rm m}11\overset{\rm s}{.}27 \pm 260$ mas,
decl. (J2000) $= +46°55'21\overset{''}{.}67 \pm 260$ mas.

3. Optical Observations and Host Galaxy Association

3.1. MMT Observations

We observed the field of FRB 20190208A using the Binospec imaging spectrograph (D. Fabricant et al. 2019) mounted on the 6.5 m MMT Observatory on 2022 May 31 UT (PI: A. Nugent; Program 2022A-UAO-G193) in the *i* band for a total of 2235 s of exposure. We used the custom `POTPyRI` pipeline[39] to apply bias and flat-field corrections, perform cosmic-ray rejection and image coaddition, and perform astrometric calibration to the Gaia DR3 catalog (Gaia Collaboration et al. 2023) on the final coadded image stack. While there are extended sources in the vicinity (Figure 3), no source was detected at the VLBI position of FRB 20190208A (determined in Section 2.5). To obtain a photometric limit at this position, we performed aperture photometry at the FRB position and the surrounding extended sources using a custom script based on the `aperture_photometry` module of `photutils` (L. Bradley et al. 2021)[40] and calculated a 3σ limit of $i \gtrsim 25.7$ mag (AB) at the position of FRB 20190208A.

We also obtained 2×900 s of spectroscopy of two sources in the field (O8 and O9; see Section 3.3 and Figure 3 for the naming convention) with MMT/Binospec, in which the slit was aligned to capture both sources. O8 was initially considered to be a plausible host, and the nearby O9 was able to be covered in the same slit. We used the 270 lines mm^{-1} grating with the LP3800 blocking filter and a central wavelength of 6500 Å to cover a wavelength range of 3850–9150 Å. The data were reduced using the Python Spectroscopic Data Reduction Pipeline (`PypeIt`; J. X. Prochaska et al. 2020a, 2020b) in the *quicklook* reduction mode to identify the redshifts of galaxies O8 and O9. For galaxy O8, we identify eight spectral features at a common redshift of $z = 0.1935 \pm 0.0203$. For galaxy O9, we identify three emission features at a common redshift of $z = 0.5473 \pm 0.0004$.

3.2. Gran Telescopio Canarias (GTC) Observations

The absence of an obvious source at the position of FRB 20190208A motivated deeper follow-up. Thus, we obtained observations with the Optical System for Imaging and low Resolution Integrated Spectroscopy (OSIRIS; J. Cepa et al. 2000) mounted on the 10.4 m GTC on 2024 June 29 and July 1 UT (PI: A. Gil de Paz; Program GTCMULTIPLE2G-24A) in the Sloan *r* band for a total of 11,520 s of exposure. The data were collected during gray time, and the seeing varied in the range $0\overset{''}{.}6$–$0\overset{''}{.}9$. The data reduction, including bias subtraction and flat-fielding, was performed using standard routines of the Image Reduction and Analysis Facility package, and the cosmic rays were removed with the L.A.Cosmic algorithm (P. G. van Dokkum 2001). We used a set of Gaia DR3 stars in the target vicinity for the astrometric calibration. The formal rms uncertainties of the astrometric solution were ΔR.A. $\sim 0\overset{''}{.}06$ and Δdecl $\sim 0\overset{''}{.}11$. We determined the photometric zero-point 28.43 ± 0.01 using several stars from the Pan-STARRS catalog (H. A. Flewelling et al. 2020). To convert their magnitudes to the Sloan Digital Sky Survey photometric system, we used the transformation equations from J. L. Tonry et al. (2012).

The resulting combined image is presented on the right-hand side of Figure 3. At the position of FRB 20190208A, we detect

[39] https://github.com/CIERA-Transients/POTPyRI
[40] https://github.com/charliekilpatrick/photometry

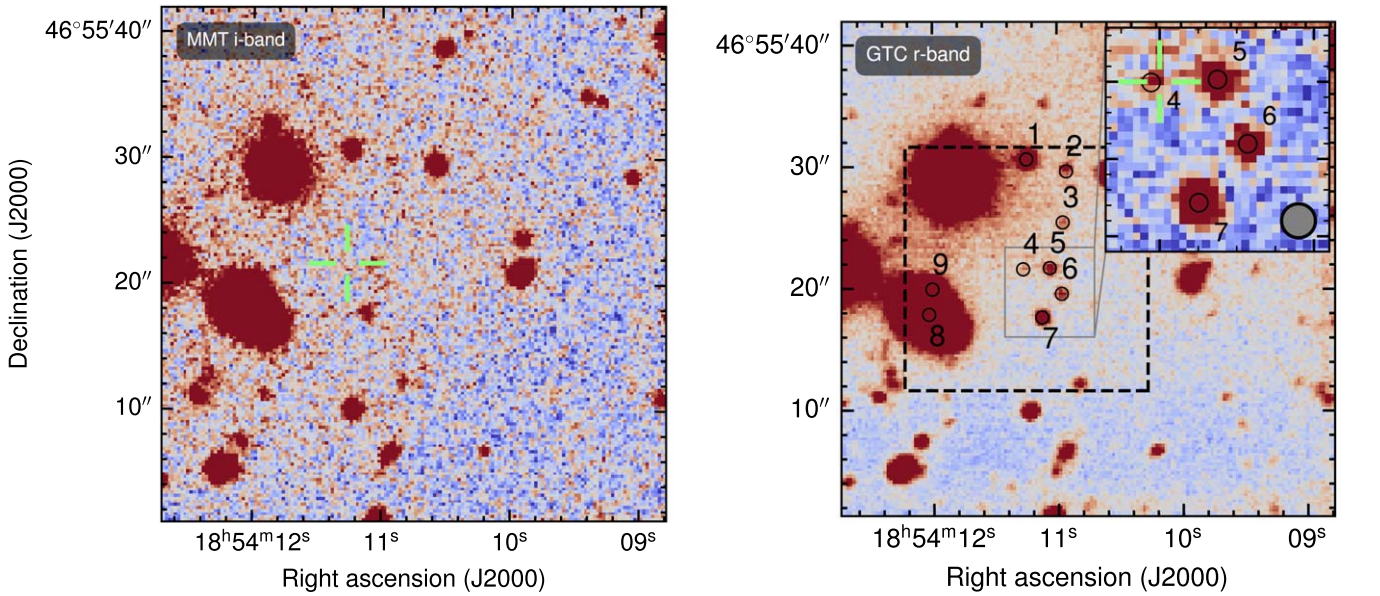

Figure 3. Left: MMT *i*-band image of the field surrounding the FRB 20190208A localization. No host is visible, with a 3σ limit of $i \gtrsim 25.7$ mag (AB) at the position of FRB 20190208A. Right: GTC *r*-band image showing the same field but achieving about 2 mag greater depth (see Section 3). The dashed black box indicates the region that was considered in host association, and the nine sources that were identified as potential candidate hosts are marked by black circles (see Section 3.3). The green crosshair indicates the FRB position—note that the EVN burst localization region is much smaller, roughly the pixel scale in this image. In the GTC image, the FRB position is spatially coincident with source O4 (also see Table 2), which is not visible in the MMT image. The gray disk in the bottom right of the inset indicates the effective point-spread function of the GTC image. The seeing varied in the range 0.″6–0.″9 during the GTC observations.

a faint unresolved source with $r = 27.32 \pm 0.16$ mag. For both the GTC and Binospec images, we perform photometry on sources O1–O9 in Figure 3, which are listed in Table 2, together with the priors and results of our Probabilistic Association of Transients to their Hosts (PATH) analysis.

3.3. Host Galaxy Association

We use PATH (K. Aggarwal et al. 2021b) to determine the most likely host galaxy. PATH is a Bayesian framework that incorporates priors on the magnitudes of surrounding galaxies, their sizes, and the transient's offset from them to calculate posteriors of association for all candidate galaxies, $P(O|x)$. We use the GTC/OSIRIS *r*-band image for this analysis, because it is the deepest image available for this field. For the magnitude prior, we use the default "inverse" prior, which gives higher weight to brighter galaxies. For the offset prior, we use the default "exponential" prior truncated at six effective radii from the galaxy candidates. Finally, we assume a value of 0.05 for the prior that the host is undetected, $P(U)$, which is a conservative assumption given the depth of the GTC image.

To select galaxy candidates, we consider a $20'' \times 20''$ region around FRB 20190208A and use `SExtractor` (E. Bertin & S. Arnouts 1996) to identify all objects that are likely galaxies per the `SExtractor` star–galaxy classifier, resulting in nine objects that we label O1–O9. We run PATH using the positions determined by `SExtractor`, photometry as described in Table 2, and estimations for the effective radii of the objects combined with our prior assumptions. O4, the object spatially coincident with the FRB source, is unambiguously favored as the host with $P(O|x) = 0.9995$; all other objects receive negligible posteriors, and the posterior on the host being undetected, $P(U|x)$, is similarly negligible at 5×10^{-5}. We report the $P(O|x)$ values for each object in Table 2 along with their magnitudes, spectroscopic redshift (if known), and offset from FRB 20190208A.

Table 2
Properties of the Host and Surrounding Galaxies of FRB 20190208A

Galaxy	*r*	Offset (arcsec)	$P(O)$	$P(O\|x)$	Redshift
O1	23.23 ± 0.02	8.97	0.054	0.0	⋯
O2	26.02 ± 0.05	8.72	0.006	0.0	⋯
O3	26.72 ± 0.09	4.95	0.004	≈0	⋯
O4	27.17 ± 0.16	0.10	0.003	0.9995	⋯
O5	25.69 ± 0.04	2.11	0.008	0.00017	⋯
O6	25.01 ± 0.05	3.72	0.006	≈0	⋯
O7	24.80 ± 0.02	4.27	0.015	≈0	⋯
O8	20.31 ± 0.02	8.70	0.790	0.00028	0.1935 ± 0.0203
O9	23.05 ± 0.05	7.74	0.063	0.0	0.5473 ± 0.0004

The host galaxy of FRB 20190208A is too faint to obtain a redshift using current ground-based spectroscopy; this might yet still be feasible with the Hubble Space Telescope or JWST. To determine a conservative upper limit on the redshift, which would allow us to constrain the maximum possible host galaxy luminosity, we calculate $P(z|\mathrm{DM})$ following J. P. Macquart et al. (2020). Throughout, we use the model parameter values used in C. W. James et al. (2020) and Planck18 cosmological parameters (Planck Collaboration et al. 2020). We account for the expected Galactic DM using a flat distribution with a ±20% spread centered on 71.5 pc cm^{-3} (from NE2001p; S. K. Ocker & J. M. Cordes 2024), the Galactic halo contribution is a flat distribution between 25 and 80 pc cm^{-3} (J. X. Prochaska & Y. Zheng 2019; S. Yamasaki & T. Totani 2020), and we fix the host DM to 0 pc cm^{-3} in order to place the most conservative limit on the maximum redshift. The field around FRB 20190208A (Figure 3) is crowded with other galaxies, implying that there might be a significant contribution to the DM from intervening circumgalactic media. We account for this by introducing scatter in the DM component from the intergalactic medium to make the final probability density

function (PDF). The PDF is plotted in Figure 5 (in orange) with the 99% confidence interval defining the maximum redshift: $z_{\rm max} \sim 0.83$. The mean of this distribution, which conservatively assumes no host contribution to the DM, is $z \sim 0.67$.

Note that scattering measurements can be used to constrain the host DM contribution under the assumption that the scattering is dominated by the host galaxy disk (J. M. Cordes et al. 2022). In our case, we have not measured a scattering timescale in the FRB 20190208A bursts but place an upper limit of $<$0.65 ms using the shortest-duration burst, B2. This upper limit is, unfortunately, not meaningfully constraining for the range of host DMs in our case, using a flat prior on the fluctuation parameter between 0.5 and 2 $(\mathrm{pc}^2\,\mathrm{km})^{-1/3}$. We compare the PDF determined following J. P. Macquart et al. (2020), plotted in orange in Figure 5, with the PDF calculated following the J. M. Cordes et al. (2022) framework, plotted in pink, using our upper limit on the scattering timescale. This highlights that the upper limit on the redshift results in a comparable galaxy luminosity ($\sim 10^8\ L_\odot$) regardless of the assumed PDF (the J. P. Macquart et al. 2020 PDF is skewed low, since it accounts for some DM contribution from intervening structure, which the J. M. Cordes et al. 2022 framework does not consider). In contrast, the lower bound on the redshift is unconstrained, since the scattering timescale does not meaningfully constrain the maximum DM host.

4. Discussion

4.1. The Importance of Precise Localization and Deep Optical Observations

The unambiguous association of FRB 20190208A to its host is due to both its 260 mas localization and the depth of the GTC image used for the PATH analysis, the combination of which are not always afforded for FRBs. To explore the sensitivity of the posteriors to the localization uncertainty for FRB 20190208A, we artificially increased the localization uncertainty region from 0.″5 to 120″, while keeping all other assumptions fixed, and noted how the posteriors changed. Figure 4 shows the $P(O|x)$ for each candidate host galaxy (with O4 being the true host) and the $P(U|x)$ as a function of localization uncertainty (radius-equivalent).

Figure 4 shows that for localization sizes $\lesssim$1″, O4 is correctly identified as the true host with $P(O|x) \gtrsim 0.8$. For a robust association, which we define as $P(O|x) \gtrsim 0.9$, a localization precision on the order of a few 100 mas, or less, is needed. Once the localization size increases to beyond a few arcseconds, the host association becomes less clear, as evident by several candidates with low but comparable $P(O|x)$. At worse precision ($\gtrsim$8″), the data begin to lose constraining power as $P(O|x)$ becomes dominated by the prior; if the localization was truly on this scale, the brightest and largest galaxy, O8, would have been identified as the host with reasonable confidence (defined as $P(O|x) \gtrsim 0.8$). This exercise highlights the importance of subarcsecond localizations in making robust associations with the true host, especially if a significant fraction of the FRB population originate from faint or low-luminosity galaxies.

In the case of FRB 20190208A, the VLBI localization, coupled with the lack of clear host within $\sim$10″ in shallower imaging, motivated extremely deep imaging. In previous PATH analyses of this system based on shallower MMT imaging, the FRB appeared significantly offset from all known candidates, as the coincident galaxy was not detected. This demonstrates that, in some cases—perhaps particularly when the FRB position is significantly offset from its putative host or apparently hostless—deep optical imaging, in addition to high-precision localization, may be necessary for a robust host association.

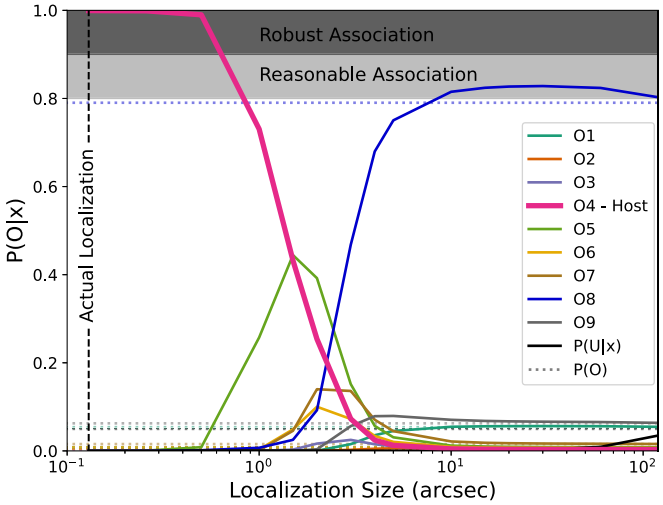

Figure 4. PATH posteriors, $P(O|x)$, for the FRB 20190208A field as a function of increasing assumed localization uncertainty (radius-equivalent). The actual 1-σ_x localization precision of the source is shown by the dashed vertical line. The $P(O|x)$ for objects O1 to O9 are represented by solid curves and their priors, $P(O)$, by horizontal dotted lines with corresponding colors (see legend). Shaded gray regions illustrate reasonable and robust host associations (defined as $P(O|x) > 0.8$ and $>$0.9, respectively).

4.2. The Implications of a Low-luminosity Dwarf Host

Figure 5 shows the r-band AB magnitude against redshift for a sample of published FRB host galaxies, including data from V. Ravi et al. (2019), M. Bhardwaj et al. (2021, 2024), A. C. Gordon et al. (2023, 2024), K. Lee-Waddell et al. (2023), F. H. Panther et al. (2023), A. L. Ibik et al. (2024), C. J. Law et al. (2024), K. M. Rajwade et al. (2024). Overplotted is the characteristic luminosity, L^* as a function of redshift, based on the Schechter galaxy luminosity function of field galaxies (P. Schechter 1976). Also shown are such curves scaled down in orders of magnitude, with data compiled from W. R. Brown et al. (2001), C. Wolf et al. (2003), C. N. A. Willmer et al. (2006), N. A. Reddy & C. C. Steidel (2009), S. L. Finkelstein et al. (2015), and K. E. Heintz et al. (2020).

The host galaxy of FRB 20190208A is very faint, less luminous than the host galaxy of FRB 20121102A ($\sim 0.01L^*$; C. G. Bassa et al. 2017; S. P. Tendulkar et al. 2017), and potentially as faint as a $\sim 0.001L^*$ galaxy, depending on the true redshift. Considering the extremes, for $z_{\rm O8} = 0.1935$ and $z_{\rm max} \sim 0.83$, the corresponding luminosities are $\sim 10^{6.8}\ L_\odot$ and $\sim 10^{8.3}\ L_\odot$, respectively. The plausible range of redshifts of the host thus implies that O4 is the lowest-luminosity FRB host galaxy to date. In future, if the redshift of O4 can be determined, it will be possible to comment on whether this host galaxy is an outlier in the FRB population or merely an extreme case still consistent with the current population of (repeating) FRB host galaxies.

In addition to FRB 20190208A and FRB 20121102A, there are a few other low-luminosity FRB hosts (for both repeating and apparently nonrepeating sources), such as the hosts of

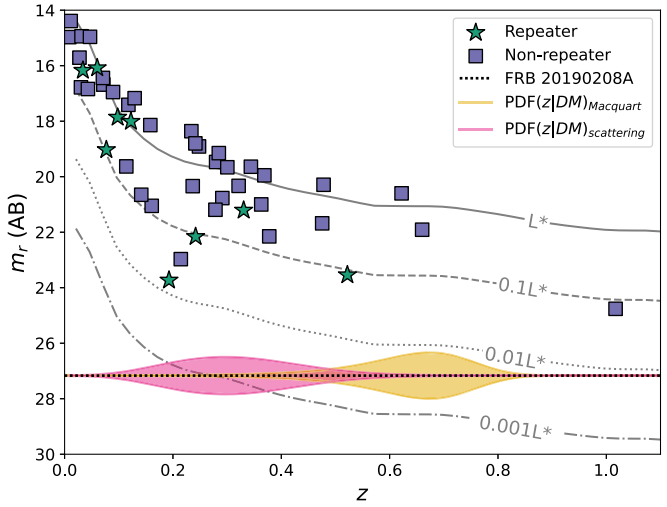

Figure 5. The r-band AB magnitude vs. inferred redshift for the host of FRB 20190208A against a background of published FRB host galaxies (references in the main text). We show the placement of L^* field galaxies and scale them in orders of magnitude down to $0.001L^*$. The true magnitude of O4 is indicated by the horizontal dashed line. Overplotted on this line are two probability density functions (PDFs) for the redshift, described in detail in Section 3.3. The orange redshift PDF indicates a conservative estimate, where $\mathrm{DM_{host}} = 0$ pc cm^{-3}, using the framework from J. P. Macquart et al. (2020). The pink redshift PDF uses an upper limit on scattering to constrain $\mathrm{DM_{host}}$, using the framework from J. M. Cordes et al. (2022). The most probable inferred redshift range for FRB 20190208A indicates that the host is consistent with a $<0.01L^*$ galaxy.

FRB 20190520B (C. H. Niu et al. 2022) and FRB 20210117A (S. Bhandari et al. 2023a). Furthermore, no host galaxy was detected for FRB 20210912A, discovered by Australian Square Kilometre Array Pathfinder (ASKAP), despite deep optical ($R > 26.7$ mag) and near-infrared ($K_s > 24.9$ mag) follow-up observations (L. Marnoch et al. 2023). These authors concluded that either the host galaxy of FRB 20210912A is intrinsically dim or the burst was exceptionally bright. If the source is situated at $z < 0.7$, it would be fainter than any FRB host galaxy previously detected. Alternatively, the host could be as luminous as or more luminous than that of FRB 20121102A, if situated further away at $z > 0.7$. The low luminosity of the host of FRB 20190208A presented in this work strengthens the feasibility of the scenario where the host of FRB 20210912A is a low-luminosity dwarf galaxy.

Recently, it has been shown that there is a significant deficit of low-mass FRB host galaxies in the local Universe (K. Sharma et al. 2024). This implies that high metallicity may play a crucial role in the production of FRB progenitors, and that FRBs may come from magnetars formed in a subpopulation of CCSNe. While various studies have shown that FRBs do not track stellar mass (K. E. Heintz et al. 2020; S. Bhandari et al. 2022; K. Sharma et al. 2024), the association of FRB 20190208A with a faint dwarf galaxy is still consistent with the host population of CCSNe, which have been proposed to be the dominant formation channel for FRB sources in the local Universe (M. Bhardwaj et al. 2024). For example, D. A. Perley et al. (2020) found that approximately 7% of CCSNe in the Zwicky Transient Facility Bright Transient Survey occur in very low-luminosity galaxies (absolute i-band magnitude $M_i > -16$ mag). Notably, the faintest Type II host galaxy in their sample, SN 2024rnu at $z = 0.032$, has $M_i = -11.84$ mag, comparable to the lower magnitude limit estimated for the host of FRB 20190208A. Similar findings have been reported by I. Arcavi et al. (2010) and K. Taggart & D. A. Perley (2021) using unbiased samples of nearby CCSN host galaxies from the Palomar Transient Factory and the All-Sky Automated Survey for Supernovae.

Alternatively, this FRB source may be one of a few outlier cases associated with extreme transients like superluminous supernovae (SLSNe) and long gamma-ray bursts (LGRBs), which predominantly occur in dwarf galaxies with high specific star formation rates (e.g., A. S. Fruchter et al. 2006; S. Savaglio et al. 2009; S. Schulze et al. 2018). The idea that FRBs may be linked to extremely massive progenitor stars, thought to be responsible for these extreme transients, was already put forward when the host galaxy of FRB 20121102A was identified as a low-metallicity dwarf (S. P. Tendulkar et al. 2017). The magnetars, hypothesized to power H-poor SLSNe (D. Kasen & L. Bildsten 2010), could potentially produce FRBs as well (B. D. Metzger et al. 2017). The preference these extreme transients have for low-mass galaxies signals that these galaxies provide certain conditions (e.g., in terms of metallicity; S. Schulze et al. 2018) that are conducive to their production. At present, we lack sufficient evidence to strongly favor either scenario.

Finally, it is worth noting that the environments of the least massive star-forming galaxies are representative of the earliest starburst galaxies in the Universe. The discovery of multiple FRBs in such galaxies could thus bode well for high-redshift FRB searches.

4.3. The Lack of a Compact PRS

Two sources of FRBs are coincident with compact PRSs with flat spectra and a spectral luminosity of $\sim 10^{29}$ erg s^{-1} Hz^{-1}: FRB 20121102A (B. Marcote et al. 2017) and FRB 20190520B (C. H. Niu et al. 2022; S. Bhandari et al. 2023b). These FRBs also have remarkably high RM values. The PRSs have been hypothesized to be magnetized neutron stars embedded in supernova remnants, wind nebulae (e.g., B. Margalit & B. D. Metzger 2018), or ultraluminous X-ray source hypernebulae (N. Sridhar & B. D. Metzger 2022). Notably, some of the most active repeaters to date (FRB 20201124A, FRB 20220912A, and FRB 20240114A) do not exhibit a PRS of similar luminosity (K. Nimmo et al. 2022b; D. M. Hewitt et al. 2024; A. Kumar et al. 2024), although G. Bruni et al. (2023) have detected a possible low-luminosity ($\sim 10^{27}$ erg s^{-1} Hz^{-1}) PRS associated with FRB 20201124A.

This low luminosity is consistent with the theoretical relation predicted between the luminosity of a PRS and RM if the PRS is the main contributor to the RM (Y.-P. Yang et al. 2020). However, this low-luminosity PRS is quite different from those associated with FRB 20121102A or FRB 20190520B. Constraints on the size are 100 times larger, the spectrum is inverted and not flat, and the host galaxy is a barred spiral as opposed to a dwarf galaxy (H. Xu et al. 2022; Y. Dong et al. 2024).

We performed a search for a PRS associated with FRB 20190208A using our EVN observations at 1.382 GHz, as well as the VLA in the C configuration at 6 GHz. With the EVN, we found no persistent radio emission on milliarcsecond scales in the 2×2 arcsec^2 region surrounding the position of FRB 20190208A. The image had an rms of 31 μJy beam^{-1}, resulting in a 5σ upper limit of 155 μJy beam^{-1} (see the left panel of Figure 8). Similarly, using the VLA image

($4\,\mu$Jy beam^{-1} rms), we could rule out the presence of a PRS above a 3σ flux density limit of $12\,\mu$Jy beam^{-1} (right panel of Figure 8). A PRS of spectral luminosity 2×10^{29} erg s^{-1} Hz^{-1} (comparable to those of FRB 20121102A and FRB 20190520B) would have a flux density of $\sim420\,\mu$Jy at $z_{\rm O8}=0.1935$ and $\sim10\,\mu$Jy at $z_{\rm max}\sim0.83$. Our data thus rule out the presence of such a luminous PRS associated with FRB 20190208A assuming reasonable redshifts.

Given the modest RM of FRB 20190208A (R. Mckinven et al. 2023; Appendices C.3 and C.4), the aforementioned RM–luminosity relation suggests a PRS luminosity of $<10^{26}$ erg s^{-1} Hz^{-1}, resulting in an expected flux density well below our detection capability even at the closest feasible redshift.

4.4. Exploring Alternative Host Scenarios

At least one repeater, FRB 20200120E (M. Bhardwaj et al. 2021), is located in a globular cluster (F. Kirsten et al. 2022). Globular clusters tend to be within a few tens of kiloparsecs from the center of their host galaxies but can also be over 100 kpc away, since they trace the dark matter halo of the host (e.g., M. Reina-Campos et al. 2022). Even in the Milky Way, there are globular clusters beyond 100 kpc from the Galactic center (W. E. Harris 1996). Alternatively, satellite galaxies in the Local Group are typically within a few hundred kiloparsecs of their hosts (see, e.g., A. W. McConnachie 2012). It thus remains plausible that the host galaxy of FRB 20190208A is a low-luminosity satellite of another galaxy in the field, or even a (very luminous) globular cluster. We discuss these options only for the galaxies for which we have measured spectroscopic redshifts, O8 and O9, although depending on the redshift of other galaxies in the field, the discussion may be applicable to them as well.

If FRB 20190208A is associated with galaxy O8 ($z=0.1935$), the impact parameter is $\sim$28 kpc. Assuming similar offsets as seen for the Milky Way, this is broadly consistent with the offsets of both satellite galaxies and globular clusters discussed above. At this redshift, a globular cluster would have to be extremely luminous, $M_r=-12.6$ mag. Perhaps the biggest challenge to association with O8 is the consequent unexplained DM excess. Having accounted for contributions from the halo and disk of the Milky Way, there would be an excess of (~300 pc cm^{-3}), comparable to the local DM contributions seen in FRB 20121102A and FRB 20190520B. However, the absence of a PRS and the lack of substantial scattering or Faraday rotation in the bursts from FRB 20190208A hints at the absence of a significant local environment contribution to the DM.

In the case of association with O9 ($z=0.547$), the large DM-excess discrepancy would be solved, and the larger impact parameter ($\sim$50 kpc) would still be consistent with the FRB 20190208A host being a satellite dwarf galaxy of O9. However, a globular cluster origin becomes implausible given the relatively large offset and, more importantly, the implied luminosity at such a distance ($M_r=-15.2$).

Lastly, further opposing a globular cluster origin, although the bursts from FRB 20200120E are similar in terms of narrowbandedness and polarimetry, they are $\sim$30 times shorter in duration and $\sim10^2$ times less luminous than those of other extragalactic FRBs (K. Nimmo et al. 2023). It is unknown whether these properties are linked to its globular cluster origin. The FRB 20190208A bursts, on the other hand, have more typical durations and spectral energies (see also E. Fonseca et al. 2020).

5. Summary

Using the EVN in EVN-Lite mode, we monitored FRB 20190208A over 3 yr, accumulating 65.6 hr of observations as part of the PRECISE campaign, and detected a single burst (B1) during this period. With the ÉCLAT monitoring campaign on the NRT, we obtained an additional 40.4 hr of exposure at $\sim$1.4 GHz, leading to the detection of one more burst (B2).

The detection of B1 enabled the VLBI localization of FRB 20190208A to R.A. (J2000) $=18^{\rm h}54^{\rm m}11\overset{\rm s}{.}27\pm260$ mas, decl. (J2000) $=+46°55'21\overset{''}{.}67\pm260$ mas. Initial optical observations with the MMT (3σ limit of $i\gtrsim25.7$ mag (AB)) revealed no host at the FRB position. Follow-up observations with the GTC revealed a faint source ($r=27.32\pm0.16$ mag) at the position of FRB 20190208A. Even the most conservative redshift estimate inferred from the DM, $z_{\rm max}\sim0.83$, indicates that the FRB 20190208A host is less luminous that the dwarf host galaxy of FRB 20121102A, making it the lowest-luminosity FRB host galaxy to date.

There has been an emerging trend where many FRB host galaxies are massive and star-forming. A low-luminosity FRB host galaxy, such as presented here, might still be consistent with the framework where the majority of FRBs are produced by magnetars formed via CCSNe but could also be part of a subpopulation where the FRB progenitor is linked to extreme transient events such as LGRBs or SLSNe (requiring low metallicity).

In the coming decade, the number of host associations will drastically increase with the advent of large-scale localization projects such as the CRACO upgrade on the ASKAP (R. M. Shannon et al. 2024), the Deep Synoptic Array (G. Hallinan et al. 2019), the Canadian Hydrogen Observatory and Radio-transient Detector (K. Vanderlinde et al. 2019), and CHIME/FRB outriggers (A. E. Lanman et al. 2024). Many scenarios may arise where localization regions are offset from potential host galaxies. In some cases, robust FRB host associations will require both high-precision localization and deep optical follow-up observations.

Acknowledgments

We thank Betsey Adams (ASTRON) for useful discussions.

The AstroFlash research group at McGill University, University of Amsterdam, ASTRON, and JIVE is supported by a Canada Excellence Research Chair in Transient Astrophysics (CERC-2022-00009), the European Research Council (ERC) under the European Union's Horizon 2020 research and innovation program ("EuroFlash"; grant agreement No. 101098079), and an NWO-Vici grant ("AstroFlash"; VI.C.192.045).

Y.D., W.F., A.C.G., and the Fong Group at Northwestern acknowledge support by the National Science Foundation under grant Nos. AST-1909358 and AST-2308182 and CAREER grant No. AST-2047919. Y.D., W.F., A.C.G., and L.M.R. acknowledge support from NSF grants AST-1911140, AST-1910471 and AST-2206490 as members of the Fast and Fortunate for FRB Follow-up team. A.K. acknowledges the DGAPA-PAPIIT grant IA105024. K.N. is an MIT Kavli fellow.

S.B. is supported by a Dutch Research Council (NWO) Veni Fellowship (VI.Veni.212.058). W.F. gratefully acknowledges support by the David and Lucile Packard Foundation, the Alfred

P. Sloan Foundation, and the Research Corporation for Science Advancement through Cottrell Scholar Award #28284. A.K. acknowledges the DGAPA-PAPIIT grant IA10502. A.G.d.P. acknowledges financial support from the Spanish Ministerio de Ciencia e Innovación under grant PID2022-138621NB-I00. F.K. acknowledges support from Onsala Space Observatory for the provisioning of its facilities/observational support. The Onsala Space Observatory national research infrastructure is funded through Swedish Research Council grant No. 2017-00648. B.M. acknowledges financial support from the State Agency for Research of the Spanish Ministry of Science and Innovation, and FEDER, UE, under grant PID2022-136828NB-C41/MICIU/AEI/10.13039/501100011033, and through the Unit of Excellence María de Maeztu 2020–2023 award to the Institute of Cosmos Sciences (CEX2019-000918-M).

Y.D. is supported by the National Science Foundation Graduate Research Fellowship under grant No. DGE-1842165. V.M.K. holds the Lorne Trottier Chair in Astrophysics & Cosmology, a Distinguished James McGill Professorship, and receives support from an NSERC Discovery grant (RGPIN 228738-13) from an R. Howard Webster Foundation Fellowship from CIFAR. K.W.M. holds the Adam J. Burgasser Chair in Astrophysics and is supported by NSF grants (2008031, 2018490). A.B.P. is a Banting Fellow, a McGill Space Institute (MSI) Fellow, and a Fonds de Recherche du Québec—Nature et Technologies (FRQNT) postdoctoral fellow. K.R.S. and V.S. are supported by FRQNT Doctoral Research Awards. K.S. is supported by the NSF Graduate Research Fellowship Program. This work was supported by the National Natural Science Foundation of China (grant Nos. 12041304 and 12288102).

This work is based in part on observations carried out using the 32 m radio telescope operated by the Institute of Astronomy of the Nicolaus Copernicus University in Toruń (Poland) and supported by a Polish Ministry of Science and Higher Education SpUB grant. This work is also based in part on observations carried out using the 32 m Badary, Svetloe, and Zelenchukskaya radio telescopes operated by the Scientific Equipment Sharing Center of the Quasar VLBI Network (Russia). We thank the directors and staff at the various participating antenna stations for allowing us to use their facilities and running the observations. The European VLBI Network (EVN) is a joint facility of independent European, African, Asian, and North American radio astronomy institutes. Scientific results from data presented in this publication are derived from EVN project code EK050.

The Nançay Radio Observatory is operated by the Paris Observatory, associated with the French Centre National de la Recherche Scientifique (CNRS).

Observations reported here were also obtained at the MMT Observatory, a joint facility of the University of Arizona and the Smithsonian Institution. MMT Observatory access was supported by Northwestern University and the Center for Interdisciplinary Exploration and Research in Astrophysics (CIERA). Part of this work is based on observations made with the Gran Telescopio Canarias (GTC), installed at the Spanish Observatorio del Roque de los Muchachos of the Instituto de Astrofísica de Canarias, on the island of La Palma.

Lastly, part of this research has made use of the EPN Database[41] of Pulsar Profiles maintained by the University of Manchester.

Facilities: EVN, NRT, VLA, MMT, GTC.

Software: AIPS (E. W. Greisen 2003), astropy (Astropy Collaboration et al. 2013), CASA (J. P. McMullin et al. 2007; I. M. van Bemmel et al. 2022), difmap (M. C. Shepherd et al. 1994), DM_phase (A. Seymour et al. 2019), DSPSR (W. van Straten & M. Bailes 2011), FETCH (D. Agarwal & K. Aggarwal 2020), heimdall,[42] IonFR (C. Sotomayor-Beltran et al. 2013), PATH (K. Aggarwal et al. 2021a), PRESTO (S. M. Ransom 2001), PolConvert (I. Martí-Vidal et al. 2016), POTPyRI,[43] PSRCHIVE (A. W. Hotan et al. 2004), PypeIt (J. X. Prochaska et al. 2020a, 2020b), scipy (P. Virtanen et al. 2020), SFXC (A. Keimpema et al. 2015), SExtractor (E. Bertin & S. Arnouts 1996).

Appendix A
EVN Observations and Data Processing

We have provided an observation log as a supplementary text file that shows all the FRB 20190208A observations conducted with a subarray of EVN dishes in "EVN-Lite" mode as part of the PRECISE FRB localization campaign. During all 38 observations, only a single burst (B1) was detected on 2021 October 17 UT (MJD 59504) in PRECISE observing run PR187A. This is also shown in Figure 6.

During PR187A, most stations recorded dual-polarization raw-voltage data with 2 bit sampling. At Irbene, only left circular polarization data were recorded. These data were in MARK5B (A. Whitney 2004) format for Svetloe, Badary, and Zelenchukskaya and VLBI Data Interchange format (A. Whitney et al. 2010) for all other stations. With the exception of Urumqi, all stations record on a circular basis. In postprocessing, linear basis polarization data from Urumqi were transformed to circular basis using the `PolConvert` program (I. Martí-Vidal et al. 2016). All stations recorded either four or eight 32 MHz subbands, as shown in Figure 7. Unfortunately, B1 occurred in a part of the band with less-than-optimal coverage, as shown by the shaded orange region of this figure.

We used the PRECISE pipeline (F. Kirsten et al. 2021) to search the raw voltages recorded at Effelsberg for bursts. First, we used `digifil` from the software suite Digital Signal Processing Software for Pulsar Astronomy (W. van Straten & M. Bailes 2011) to create Stokes I filter-bank data from the raw-voltage data, with time and frequency resolutions of 64 μs and 62.5 kHz, respectively. We then searched these filter-bank data over a DM range of 529–629 pc cm^{-3} for transient signals above a signal-to-noise ratio (S/N) threshold of 7 using the transient-detection software `Heimdall`.[44] Thereafter, the pipeline fed the candidates from the search to `FETCH` (D. Agarwal & K. Aggarwal 2020), a machine learning convolutional neural network that assigns a probability that a given transient signal is astrophysical in origin using various deep-learning models. In the PRECISE project, we have empirically determined that the `FETCH` models "A" and "H" complement each other well in terms of completeness and number of false positives. Finally, we manually inspected all the candidates for which either of these two models assigned a probability of higher than 0.5 of being astrophysical.

In the first correlation pass at JIVE with `SFXC` (A. Keimpema et al. 2015), all nontarget scans were correlated with the

[41] https://psrweb.jb.man.ac.uk/epndb/

[42] sourceforge.net/projects/heimdall-astro/

[43] https://github.com/CIERA-Transients/POTPyRI

[44] sourceforge.net/projects/heimdall-astro/

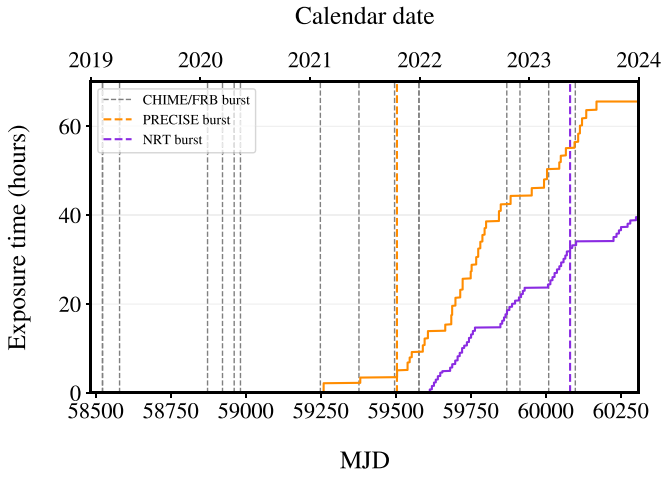

Figure 6. All known bursts. detected from FRB 20190208A are indicated by dashed vertical lines. Bursts detected by CHIME/FRB are indicated in gray, while the bursts detected by PRECISE (B1) and ÉCLAT (B2) are in orange and purple, respectively. The MJD is shown on the bottom axis and the corresponding calendar date on the top axis. The solid orange curve shows the cumulative time (in hours) that FRB 20190208A has been observed by PRECISE, while the solid purple shows the same but for the ÉCLAT project on the NRT.

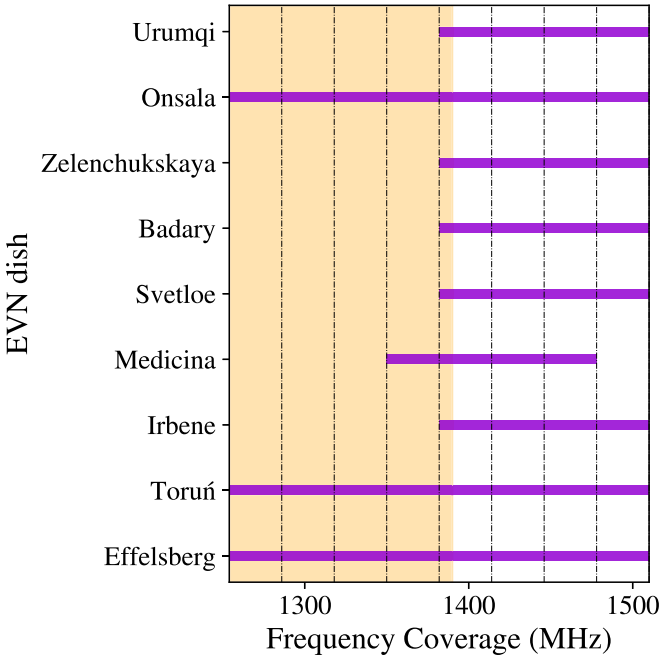

Figure 7. The frequency coverage for different antennas in our PRECISE observations are shown here by horizontal purple bars. The edges of subbands are indicated by dashed black vertical lines. The shaded orange region indicates the spectral extent of burst B1.

standard 2 s integration time and 8×32 MHz subbands, consisting of 64 channels each. These data were used to provide an accurate calibration that could be applied to the burst data correlated in the following passes. Initially, FRB 20190208A's position (derived from the CHIME/FRB baseband data) was only known with arcminute precision, and we used this position as the phase center in our initial correlations: R.A. (J2000) = $18^{\rm h}54^{\rm m}09\overset{\rm s}{.}4320$, decl. (J2000) = $46°55'34\overset{''}{.}680$. In order to first establish the burst position to an uncertainty of about $1''$, burst B1 was coherently dedispersed (intrachannel dedispersion) using a DM of 580.467 pc cm^{-3} before a correlation gate was selected manually around the arrival time of B1 to optimize the S/N. We then derived the delay residuals for each baseline by fringe-fitting these data; the delay residuals are proportional to the angular offset between the burst position and the phase center. This method is known as delay mapping. A detailed description of this technique has previously been presented in B. Marcote et al. (2020). Using the delay-mapping position as the phase center, a second correlation pass was conducted on the burst data to finally image the burst. In the third and final correlation pass, all target scans were correlated using the same time and frequency integration as for the calibrators for deep imaging to search for persistent radio emission using the same position for the target as derived from the burst correlation.

To calibrate and image the correlated EVN data, we used `AIPS` (E. W. Greisen 2003) and `DIFMAP` (M. C. Shepherd et al. 1994). These procedures have also been described in previous PRECISE localization papers (e.g., B. Marcote et al. 2020), but we repeat them here for the sake of completeness and convenience. The EVN provides the correlated visibilities in FITS-IDI format, together with calibration pipeline products. We first loaded these correlated visibilities into `AIPS` before applying the calibration table containing the a priori gain correction and parallactic angle correction, the a priori flagging table, and the bandpass calibration table. We then manually flagged the radio frequency interference (RFI) in the fringe finder (J1419+5423) scan and the edges of each subband where the signal becomes weaker (∼15% of the data). Next, we corrected for ionospheric dispersive delays using Jet Propulsion Laboratory maps of total electron content during the observation at the different EVN sites. Each subband has a different signal path that induces phase jumps between subbands, as well as phase slopes within them. With Effelsberg as a reference antenna, we used the fringe finder scan to correct for these instrumental delays. Thereafter, we performed a global fringe fit, using the fringe finder and phase calibrator (J1852+4855), to correct the delays and rates of the phases, as a function of both time and frequency, for all the calibrators during the entire observation. We manually inspected the solutions and flagged those where the calibration failed. These solutions were applied to the check source (J1850+4959) for verification and then to the target field before imaging.

In previous PRECISE localizations, the uncertainty on the FRB position was taken to be the quadrature sum of multiple factors: the statistical uncertainty derived from the shape and size of the synthesized beam normalized by the S/N, the statistical uncertainty on the position of the phase calibrator, an estimate of the uncertainty from phase referencing due to the angular separation between the phase calibrator and FRB, an estimate of the frequency-dependent shift in the phase calibrator position from the International Celestial Reference Frame, and the statistical uncertainty on the positions of the interferometric check source. All of these contributions are typically on the order of milliarcseconds or less, and the total uncertainty was often dominated by the phase-referencing uncertainty estimate.

This approach is effective when the visibilities of multiple bursts can be stacked to obtain sufficient *uv*-coverage for a single point source to become visible in the dirty map. The precision to which the FRB position is then known is approximately equivalent to 20% of the synthesized beam size. With poor *uv*-coverage side lobes becoming large in

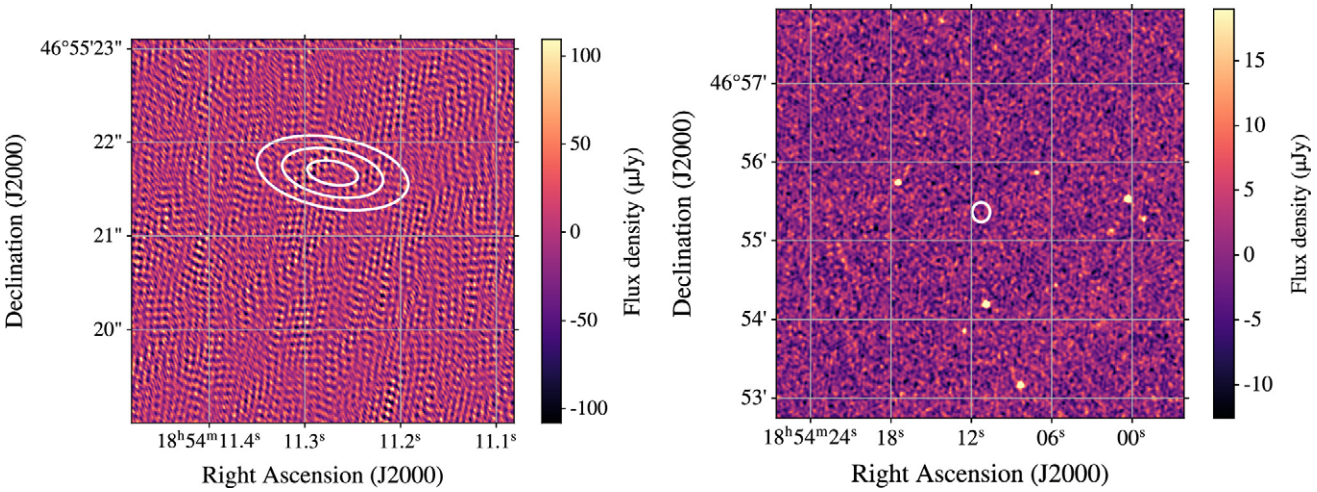

Figure 8. Radio continuum maps from our 1.4 GHz EVN observations (uncleaned; left) and the VLA observations in C configuration at 6 GHz (cleaned; right) to search for persistent radio emission. The rms is 31 and 4 μJy beam^{-1} for the EVN and VLA images, respectively. The ellipses in the EVN image are centered on the VLBI position of FRB 20190208A and are described in Section 2.5. The white circle in the VLA image also indicates the FRB position but is much larger than the aforementioned ellipses. We find no PRSs associated with FRB 20190208A.

amplitude, and while the addition of amplitudes will cause the S/N of different side lobes to vary, the addition of phases can cause the entire fringe pattern to shift. This means that the true FRB position is not necessarily on top of a local maximum of a side lobe. Due to the ambiguity in the case of FRB 20190208A presented here, we conservatively transform $2 \times \sigma_y$ of the 2D Gaussian fit into the R.A. and decl. reference frame to obtain a quasi-positional error on the FRB position.

Appendix B
NRT Observations and Data Processing

In the supplementary materials, we have provided an observation log of the observations from the ÉCLAT FRB monitoring campaign on the NRT of FRB 20190208A. Only a single burst (B2) was detected on 2023 May 17 UT (MJD 60081).

The data recorded by NUPPI were searched for bursts using the ÉCLAT pipeline, which has been described in more detail in D. M. Hewitt et al. (2023). In short, the eight 32 bit, 64 MHz full-polarization subbands recorded by NUPPI were spliced together and converted into 8 bit, 512 MHz Stokes *I* filter-bank data, which were then passed in 2 minute blocks to `rfifind` from the pulsar software suite PRESTO (S. M. Ransom 2001). Once the most RFI-contaminated channels were identified, we masked these channels but refrained from any temporal masking. Using `Heimdall`, these masked filter-bank data were searched for candidates above an S/N of 7. The DM search range used for FRB 20190208A is 558–609 pc cm^{-3} (the data were coherently dedispersed to a DM of 579 pc cm^{-3} within each 4 MHz channel). Notably, we searched for candidates down to the native time resolution of the data (16 μs). Afterward, the `FETCH` models "A"–"H" classified the candidates as being astrophysical in origin, and all candidates for which any model assigned a score above 0.5 were manually inspected. In the event that bursts are detected, they are extracted with full polarization information from the 32 bit raw data. These extracted data are used for all subsequent analyses.

Appendix C
Burst Analysis

In Table 1, we tabulated the properties of bursts B1 and B2. The temporal burst widths and spectral extents quoted are the FWHM of Gaussian fits to the frequency- and time-averaged data, respectively. We calculate fluences by first multiplying the normalized frequency-averaged burst profiles (where noise has a mean of 0 and standard deviation of 1) with the radiometer equation to convert to physical units and then integrating over the extent of the burst in time and the *entire* observing band. The system temperature and gain for the NRT at 1.4 GHz are approximately 35 K and 1.4 K Jy^{-1}, respectively. The system temperature and gain for Effelsberg are 20 K and 1.4 K Jy^{-1}, respectively. We assume these values, and by extension our fluences, to have an uncertainty of approximately 20%.

C.1. DM Determination

Accurate DM determination in the absence of prominent burst structure or short-timescale features is nontrivial. In these cases, the DM will likely be overestimated since the intraburst time–frequency drift (J. W. T. Hessels et al. 2019) cannot easily be disentangled from dispersion, and S/N will be optimized for rather than structure. To determine the DM, we made use of both S/N-optimization and structure-optimization approaches. For B1, we have baseband data and thus generated a filter-bank data set, coherently dedispersed to a preliminary DM of 579.8 pc cm^{-3}, with 8 μs time resolution and 250 kHz frequency resolution. This preliminary DM is similar to the DM of FRB 20190208A bursts found by CHIME/FRB around the same period of time (R. Mckinven et al. 2023). For B2, the burst data we used for this analysis had the native time and frequency resolution (16 μs and 4 MHz) that was recorded at NRT, coherently dedispersed to a DM of 579 pc cm^{-3} used in the search pipeline. For both B1 and B2, we first flag any channels contaminated by RFI before performing the analysis.

In order to optimize for S/N, we incoherently dedispersed the bursts to a range of DMs between 577 and 583 pc cm^{-3}. For each DM trial, we measured the peak S/N of the profile obtained

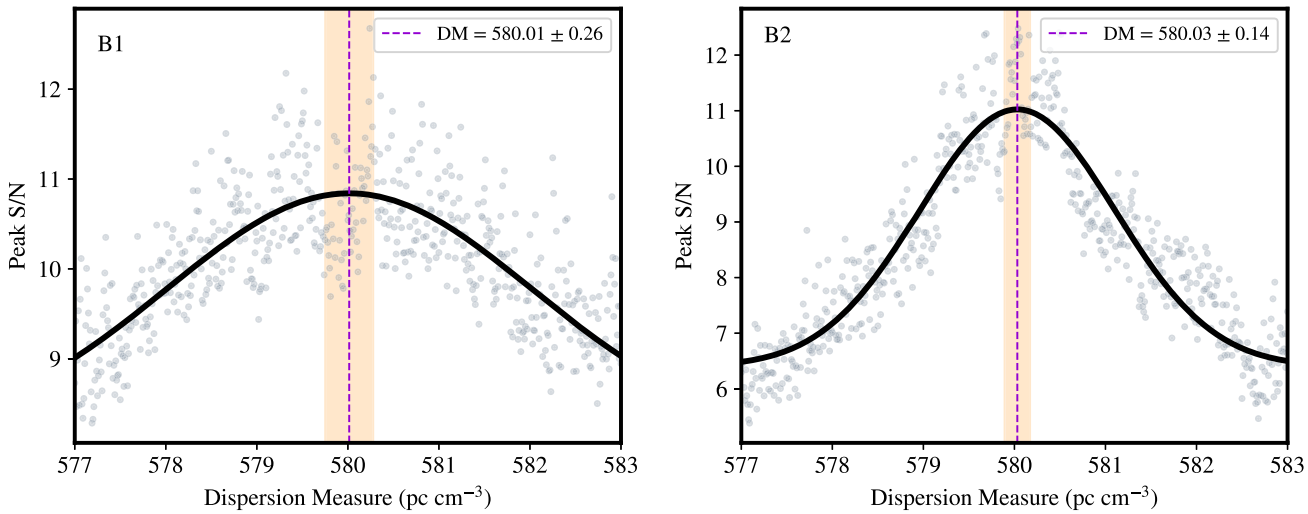

Figure 9. DM determination by S/N optimization for bursts B1 (left) and B2 (right). The gray data points denote the peak S/N at various DM trials. A Gaussian fit to the data is shown in black. The center of the Gaussian and its 3σ error are indicated by the vertical dashed purple lines and the shaded orange regions, respectively.

by averaging the channels where the burst is present. We then performed a bootstrap fit of a Gaussian function to the S/N-versus-DM curve to quantify the best DM and estimate the uncertainty, finding best DMs of 580.01 ± 0.26 and 580.03 ± 0.14 pc cm^{-3} for B1 and B2, respectively (Figure 9).

In order to optimize for burst structure, we made use of `DM_phase` (A. Seymour et al. 2019) and considered only the part of the observing band where the burst is visible while also limiting fluctuation frequencies to below 0.75 m s^{-1}. The resulting DMs for B1 and B2 are 580.24 ± 0.23 and 579.84 ± 0.29 pc cm^{-3}, respectively.

The results from both methods are consistent within the uncertainties for both bursts B1 and B2, suggesting that both bursts lack any prominent substructure on submillisecond timescales. For the remainder of analyses in this work, we will use DMs of 580.1 and 579.9 pc cm^{-3} for bursts B1 and B2, respectively. For the Effelsberg data, the smearing in the lowest 250 kHz channel, if no coherent dedispersion is applied, is 0.6 ms. We thus create a filter-bank data set for B1, coherently dedispersed to a DM of 580.1 pc cm^{-3} to mitigate the DM smearing. The NRT data for FRB 20190208A were already coherently dedispersed to a DM of 579 pc cm^{-3} at the time of recording. This difference of 0.9 pc cm^{-3} results in a temporal smearing of $\sim$16 μs at the lowest-frequency channel, which is equivalent to the time resolution of our data and consequently negligible.

C.2. Scattering, Scintillation, and High-time-resolution Analysis

FRBs can be asymmetrically temporally broadened through scattering, induced by screens of turbulent media along the line of sight to the source (e.g., K. Nimmo et al. 2024). The estimated extragalactic pulse broadening (τ_X) along the line of sight toward FRB 20190208A is 0.499 μs at 1 GHz (NE2001p; J. M. Cordes & T. J. W. Lazio 2002; S. K. Ocker & J. M. Cordes 2024). Assuming a $\tau \propto \nu^{-4}$ scaling, the corresponding expected scattering timescales at the center frequencies of our PRECISE (1382 MHz) and NRT (1484 MHz) observations are 0.137 and 0.103 μs, respectively. This is much smaller than the time resolution of our NRT observations, and we see no prominent scattering tail in either B1 or B2. CHIME/FRB has reported scattering times of $<$1.8 ms at 600 MHz for FRB 20190208A bursts (E. Fonseca et al. 2020). The scaled expectation from NE2001 is 3.850 μs.

Alternatively, these scattering screens can also induce scintillation in the FRB spectra. While there is also no prominent scintillation visible by eye in the dynamic spectra of B1 and B2, the expected scintillation bandwidth at 1 GHz along this line of sight is 0.37 MHz (NE2001p; J. M. Cordes & T. J. W. Lazio 2002; S. K. Ocker & J. M. Cordes 2024). Scaling (using $\nu_{sb} \propto \nu^4$) to the central frequencies of our observations yields 1.35 MHz at 1382 MHz and 1.79 MHz at 1484 MHz. We thus expect the scintillation bandwidth to be detectable in B1 (raw-voltage data), while for the B2 data, the frequency resolution (4 MHz) is insufficient to resolve the expected frequency scale. If there are multiple scattering screens along the line of sight (see, e.g., M. W. Sammons et al. 2023), the corresponding characteristic frequency scales of the different screens should be present in the autocorrelation function (ACF; if there is sufficient resolution to resolve them). For B1, we produced filter-bank data sets from the raw-voltage data recorded at Effelsberg with different frequency resolutions and computed the ACFs using an implementation of `fftconvolve` from the scipy.signal package. We then fit a Lorentzian function to the ACFs of the normalized, time-averaged FRB spectrum to measure the scintillation bandwidth (defined as the half-width at half-maximum of this Lorentzian fit; see, e.g., B. J. Rickett 1990). We found no evidence for a frequency scale around the frequency lag corresponding to the expected scintillation bandwidth ($\sim$1.35 MHz). Instead, we measure a scintillation bandwidth of approximately 0.1 MHz, more than an order of magnitude lower than the expectation. The ACFs of B1 at different frequency resolutions are shown in Figure 10.

The lack of substantial scattering and scintillation in the bursts from FRB 20190208A suggests that the bursts are not heavily modulated by propagation effects other than dispersion. Motivated by the presence of submillisecond time structure in bursts from other repeating FRBs (e.g., K. Nimmo et al. 2021, 2022a; D. M. Hewitt et al. 2023), we investigate to see if these FRB 20190208A bursts contain such structure. Again we

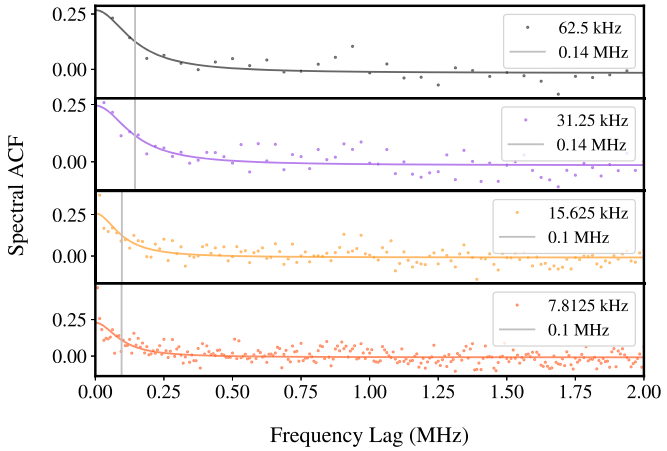

Figure 10. The time-averaged spectral ACF of B1 at different frequency resolutions (quoted in each panel). Lorentzian fits have been overplotted in colored lines, while the vertical gray line in each panel indicates the measured scintillation bandwidth for that frequency resolution.

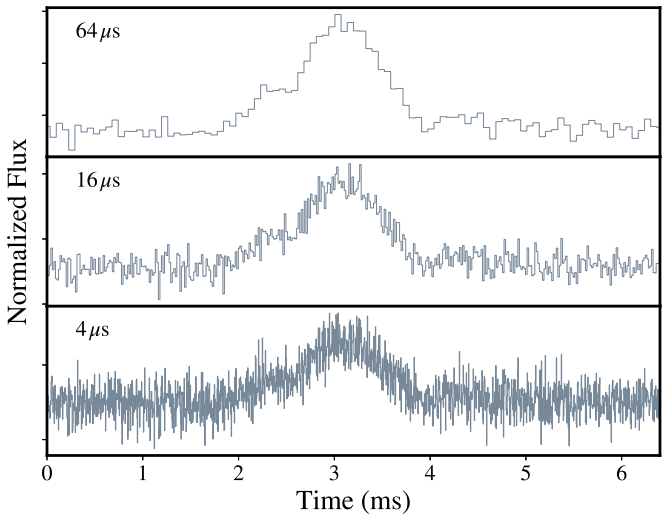

Figure 11. The frequency-averaged time profile of B1 at different time resolutions. In each case, the burst has been coherently dedispersed to a DM of 580.1 pc cm^{-3}.

generated filter-bank data sets, coherently dedispersing to a DM of 580.1 pc cm^{-3} (see Appendix C.1), with time resolutions of 64, 16, and 4 μs. As can be seen in Figure 11, we find no significant temporal structure when probing B1 at these time resolutions.

Interestingly, while B1 and B2 differ by about a factor of 2 in duration, both have similar temporal morphology, showing a small shoulder on the leading side of the burst.

C.3. Polarimetry: Effelsberg

Following K. Nimmo et al. (2021), we use a test pulsar (the 5 minute scan of PSR B2255+58 in this case) instead of noise diode data to calibrate the polarimetry of our observations. Since the RM and levels of linear and circular polarization of the pulsar are confidently measured (see, e.g., J. H. Seiradakis et al. 1995), we determine the calibration solutions required to reproduce the polarimetric properties of the test pulsar and then also apply these solutions to the FRB data.

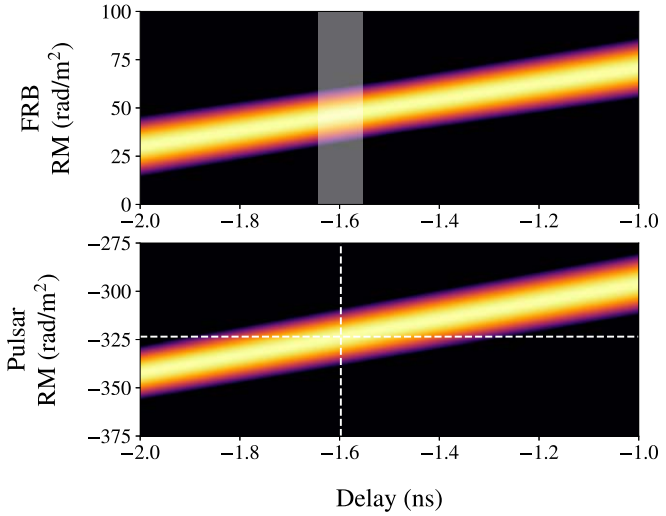

Figure 12. The RM spectra of FRB 20190208A (top) and PSR B2255+58 (bottom) as a function of instrumental delay. The color map has been saturated at the normalized 90% power level. The horizontal dashed line in the bottom panel indicates the known RM of the pulsar, and the vertical line is the corresponding delay value. In the top panel, the shaded white region shows the range of delays corresponding to a 2 rad m^{-2} deviation in pulsar RM.

Our uncalibrated pulsar data showed negligible levels of circular polarization, in contrast to ∼5% of circular polarization seen from the known profile (e.g., D. M. Gould & A. G. Lyne 1998). We interpreted this as leakage between the two polarization hands, since the Effelsberg receiver has a circular basis (Stokes V = RR − LL). By systematically exploring a range of values, we determined that the leakage correction required to reproduce the known circular polarization profile was approximately 5%. After correcting for this, we ignore second-order effects and assume the only two factors that affect Stokes Q and U are Faraday rotation and a frequency-independent delay between the polarization hands. We performed a brute-force search for the instrumental delay, given the known RM of the pulsar (−323.5 rad m^{-2}; ATNF Pulsar Catalogue;[45] R. N. Manchester et al. 2005), and found a best-fit delay of -1.598 ± 0.03 ns. To illustrate the dependency between delay and RM, we generated Faraday spectra (RM range −2000 to 2000 rad m^{-2}) for a range of delays between −20 and 20 ns. In Figure 12, we show a region of this parameter space zooming in on the area surrounding the known RM of our pulsar and its corresponding delay.

We proceeded to calibrate the FRB data, first applying the aforementioned leakage correction, before generating the same RM-delay plot for burst B1. Given our best delay found from analyzing the pulsar, the corresponding optimal RM for B1 is $+46.5 \pm 16.5$ rad m^{-2}. To estimate the uncertainty on the RM of B1, we first assume a potential deviation of ± 2 rad m^{-2} in the RM of the pulsar (nearly double the expected ionospheric contribution). This translates to a small range of delays, indicated by the white shaded region in the top panel of Figure 12, which in turn translates to a range of potential RMs for B1. We took this range of RMs (measured at the 90% power level of the Faraday spectra) as the final error estimate.

After correcting the FRB data for this optimal RM, we calculated the linear and circular polarization levels. As for many repeater bursts (e.g., K. Nimmo et al. 2022a, and

[45] www.atnf.csiro.au/research/pulsar/psrcat/

references therein), the burst is nearly 100% linearly polarized, shows negligible levels of circular polarization, and has a flat PPA across its duration (Figure 1).

C.4. Polarimetry: NRT

To determine the polarization properties and RM of burst B2, we calibrated both the burst and a short observation of the pulsar PSR B0031−07 with PSRCHIVE tools (A. W. Hotan et al. 2004). We used the pac command with the complete RECEPTION calibration model (W. van Straten 2004, 2013), which also takes into account the ellipticities and orientations of the polarization hands to model the response of a receptor with nonideal feeds. Our implementation makes use of a polarization calibration modeling file, which is generated from a 1 hr observation of the pulsar J0742−2822 during which the receiver horn is rotated by 180°. This mimics wide parallactic angle variation allowing for the implementation of the RECEPTION model (L. Guillemot et al. 2023).

The polarization properties of PSR B0031−07 slightly vary across our NRT observing window. Nevertheless, our calibration enabled us to reproduce the polarization profile at 1369 MHz (S. Johnston & M. Kerr 2018) and 1642 MHz (D. M. Gould & A. G. Lyne 1998). Using PSRCHIVE's rmfit, we found an RM of 9.40 ± 3.75 rad m^{-2} for PSR B0031−07, consistent with the known value of 9.89 rad m^{-2} (R. N. Manchester et al. 2005). Having confirmed that our calibration was successful, we applied the same technique to burst B2, resulting in an RM of -5.2 ± 4.9 rad m^{-2}. The resulting polarization profile after correcting for this RM is shown in panels (a) and (b) of Figure 1 (right). As with B1, the burst is nearly 100% linearly polarized and nearly 0% circularly polarized and has a constant PPA.

C.5. Constraints on Frequency-dependent Activity

In Table 3, we tabulate the fluence thresholds, total observing time, and burst rates using Poissonian statistics for the PRECISE, ÉCLAT, and CHIME/FRB (CHIME/FRB Collaboration et al. 2023) observations. We note here that the repetition rates for the different telescopes are not calculated over the same time period (Figure 6). We calculated the fluence thresholds, $F_{\rm th}$, by assuming a $t = 1$ ms burst and using the following adaptation of the radiometer equation:

$$F_{\rm th} = {\rm S/N} \times {\rm SEFD} \times \sqrt{\frac{t}{n_{\rm pol}\,\Delta\nu}}. \quad \text{(C1)}$$

Here, S/N is the signal-to-noise threshold used in burst searches, SEFD is the system equivalent flux density (approximately 25 Jy for the NRT and 14 Jy for Effelsberg at ∼1.4 GHz), $n_{\rm pol}$ is the number of polarizations recorded (two in these cases), and $\Delta\nu$ is the observing bandwidth.

At first glance, the burst rates might seem comparable given the large uncertainties; however, there is a more than an order of magnitude difference in the fluence thresholds between low- and high-frequency detections, and the bursts presented here are below the fluence threshold of CHIME/FRB.

To better compare the burst rates at different frequencies, we calculate the statistical spectral index, $\alpha_{\rm s}$, following the formalism presented in L. J. M. Houben et al. (2019) and also adopted in P. Chawla et al. (2020). Assuming that burst energies at a given frequency (ν) follow a statistical distribution that can be described by a power law, the frequency-specific differential energy distribution of an FRB source is then given by $dN(\nu)/dE = A(\nu)\ E^{\gamma}$, where the power-law index, γ, is assumed to be constant over frequency and time. The statistical spectral index, $\alpha_{\rm s}$, is the power-law index relating the normalization factor $A(\nu)$ of the differential energy distribution of an FRB source at different frequencies.

Taking into account the fluence thresholds of two different instruments, $F_{\nu_1,\rm min}$ and $F_{\nu_2,\rm min}$, operating at two different frequencies, ν_1 and ν_2, the burst repetition rates, λ_1 and λ_2, are related as follows:

$$\frac{\lambda_1}{\lambda_2} = \left(\frac{\nu_1}{\nu_2}\right)^{-\alpha\gamma}\left(\frac{F_1}{F_2}\right)^{\gamma+1}. \quad \text{(C2)}$$

Importantly, this assumes that the repetition rates are constant with time. To then calculate $\alpha_{\rm s}$, we performed 10,000 trials, sampling different values for the repetition rates and γ and solving for $\alpha_{\rm s}$. The repetition rates were sampled within the 90% confidence intervals and γ from a Gaussian distribution with mean −2.5 and standard deviation 0.5, which contains the wide range of values of γ measured in the literature (e.g., L. J. M. Houben et al. 2019; J. P. Macquart et al. 2019; P. Chawla et al. 2020; A. E. Lanman et al. 2022). This resulted in distributions of $\alpha_{\rm s}$, from which we determined the 95% confidence interval. For FRB 20190208A, we find $\alpha_{\rm s,NRT/CHIME} = -2.30 \pm 0.46$ and $\alpha_{\rm s,EFF/CHIME} = -2.96 \pm 0.49$, using the detections from the ÉCLAT and PRECISE observations, respectively, as referenced to the CHIME/FRB detections.

These values are largely consistent within the errors to what has been estimated for FRB 20121102A in the comparable 1.2–3.5 GHz frequency range by L. J. M. Houben et al. (2019) and only negligibly steeper than that for FRB 20180916B in the slightly lower 0.3–0.8 GHz frequency range by P. Chawla et al. (2020). Notably, the sign of $\alpha_{\rm s}$ is consistently negative for all three of these repeating sources, implying decreasing bursting activity with increasing frequency. Future measurements using detections spanning wider frequency ranges can inform us if this index remains constant over the whole range of frequencies that the sources are detected at or if any flattening and/or steepening is observed at relatively lower and/or higher frequencies.

Table 3
Technical Specifications and Detection Rates of Different Monitoring Campaigns on FRB 20190208A

	CHIME/FRB[a]	Effelsberg	NRT
Total observation time[b] (hr)	⋯	65.59	40.42
Fluence threshold (Jy ms)	5	0.13	0.17
Frequency range (MHz)	400–800	1254–1510	1228–1740
Number of bursts detected	15	1	1
Burst rate[c] ($\times 10^{-2}$ bursts hr^{-1})	$4.34^{+3.81}_{-2.30}$	$1.5^{+5.7}_{-1.5}$	$2.5^{+9.3}_{-2.4}$

Notes.
[a] Values from CHIME/FRB Collaboration et al. (2023).
[b] For Effelsberg and the NRT, these are the total observation times of FRB 20190208A from the PRECISE and ÉCLAT campaigns, respectively, up until the end of 2023.
[c] These rates are not calculated over the same time period.

ORCID iDs

Danté M. Hewitt https://orcid.org/0000-0002-5794-2360
Mohit Bhardwaj https://orcid.org/0000-0002-3615-3514
Alexa C. Gordon https://orcid.org/0000-0002-5025-4645
Aida Kirichenko https://orcid.org/0000-0002-8139-8414
Kenzie Nimmo https://orcid.org/0000-0003-0510-0740
Shivani Bhandari https://orcid.org/0000-0003-3460-506X
Ismaël Cognard https://orcid.org/0000-0002-1775-9692
Wen-fai Fong https://orcid.org/0000-0002-7374-935X
Armando Gil de Paz https://orcid.org/0000-0001-6150-2854
Akshatha Gopinath https://orcid.org/0000-0002-1836-0771
Jason W. T. Hessels https://orcid.org/0000-0003-2317-1446
Franz Kirsten https://orcid.org/0000-0001-6664-8668
Benito Marcote https://orcid.org/0000-0001-9814-2354
Vladislavs Bezrukovs https://orcid.org/0000-0003-3655-2280
Richard Blaauw https://orcid.org/0000-0003-1771-1012
Justin D. Bray https://orcid.org/0000-0002-0963-0223
Salvatore Buttaccio https://orcid.org/0000-0002-3341-466X
Tomas Cassanelli https://orcid.org/0000-0003-2047-5276
Pragya Chawla https://orcid.org/0000-0002-3426-7606
Alessandro Corongiu https://orcid.org/0000-0002-5924-3141
William Deng https://orcid.org/0009-0002-1304-0346
Yuxin Dong https://orcid.org/0000-0002-9363-8606
Marcin P. Gawroński https://orcid.org/0000-0003-4056-4903
Marcello Giroletti https://orcid.org/0000-0002-8657-8852
Lucas Guillemot https://orcid.org/0000-0002-9049-8716
Jeff Huang https://orcid.org/0000-0002-8043-0048
Dmitriy V. Ivanov https://orcid.org/0000-0002-9270-5926
Ronniy C. Joseph https://orcid.org/0000-0003-3457-4670
Victoria M. Kaspi https://orcid.org/0000-0001-9345-0307
Mikhail A. Kharinov https://orcid.org/0000-0002-0321-8588
Mattias Lazda https://orcid.org/0000-0002-5857-4264
Michael Lindqvist https://orcid.org/0000-0002-3669-0715
Giuseppe Maccaferri https://orcid.org/0000-0002-1482-708X
Lluis Mas-Ribas https://orcid.org/0000-0003-4584-8841
Kiyoshi W. Masui https://orcid.org/0000-0002-4279-6946
Ryan Mckinven https://orcid.org/0000-0001-7348-6900
Alexey Melnikov https://orcid.org/0000-0002-8466-7026
Daniele Michilli https://orcid.org/0000-0002-2551-7554
Andrey G. Mikhailov https://orcid.org/0000-0002-3355-2261
Anya E. Nugent https://orcid.org/0000-0002-2028-9329
Omar S. Ould-Boukattine https://orcid.org/0000-0001-9381-8466
Zsolt Paragi https://orcid.org/0000-0002-5195-335X
Aaron B. Pearlman https://orcid.org/0000-0002-8912-0732
Ue-Li Pen https://orcid.org/0000-0003-2155-9578
Ziggy Pleunis https://orcid.org/0000-0002-4795-697X
Ketan R. Sand https://orcid.org/0000-0003-3154-3676
Vishwangi Shah https://orcid.org/0000-0002-4823-1946
Kaitlyn Shin https://orcid.org/0000-0002-6823-2073
Mark P. Snelders https://orcid.org/0000-0001-6170-2282
Tiziana Venturi https://orcid.org/0000-0002-8476-6307
Na Wang https://orcid.org/0000-0002-9786-8548
David R. A. Williams-Baldwin https://orcid.org/0000-0001-7361-0246
Jun Yang https://orcid.org/0000-0002-2322-5232

References

Agarwal, D., & Aggarwal, K. 2020, FETCH: Fast Extragalactic Transient Candidate Hunter, Astrophysics Source Code Library, ascl:2005.014
Aggarwal, K., Agarwal, D., Lewis, E. F., et al. 2021a, ApJ, 922, 115
Aggarwal, K., Budavári, T., Deller, A. T., et al. 2021b, ApJ, 911, 95
Arcavi, I., Gal-Yam, A., Kasliwal, M. M., et al. 2010, ApJ, 721, 777
Astropy Collaboration, Robitaille, T. P., Tollerud, E. J., et al. 2013, A&A, 558, A33
Bassa, C. G., Tendulkar, S. P., Adams, E. A. K., et al. 2017, ApJL, 843, L8
Bertin, E., & Arnouts, S. 1996, A&AS, 117, 393
Bhandari, S., Gordon, A. C., Scott, D. R., et al. 2023a, ApJ, 948, 67
Bhandari, S., Heintz, K. E., Aggarwal, K., et al. 2022, AJ, 163, 69
Bhandari, S., Marcote, B., Sridhar, N., et al. 2023b, ApJL, 958, L19
Bhardwaj, M., Gaensler, B. M., Kaspi, V. M., et al. 2021, ApJL, 910, L18
Bhardwaj, M., Michilli, D., Kirichenko, A. Y., et al. 2024, ApJL, 971, L51
Bochenek, C. D., Ravi, V., Belov, K. V., et al. 2020, Natur, 587, 59
Bradley, L., Sipőcz, B., Robitaille, T., et al. 2021, astropy/photutils: v1.3.0, Zenodo, doi:10.5281/zenodo.5796924
Brown, W. R., Geller, M. J., Fabricant, D. G., & Kurtz, M. J. 2001, AJ, 122, 714
Bruni, G., Piro, L., Yang, Y.-P., et al. 2023, Natur, 632, 1014
Cepa, J., Aguiar, M., Escalera, V. G., et al. 2000, Proc. SPIE, 4008, 623
Chawla, P., Andersen, B. C., Bhardwaj, M., et al. 2020, ApJL, 896, L41
CHIME/FRB Collaboration, Andersen, B. C., Bandura, K. M., et al. 2020, Natur, 587, 54
CHIME/FRB Collaboration, Andersen, B. C., Bandura, K., et al. 2023, ApJ, 947, 83
Chittidi, J. S., Simha, S., Mannings, A., et al. 2021, ApJ, 922, 173
Cordes, J. M., & Lazio, T. J. W. 2002, arXiv:astro-ph/0207156
Cordes, J. M., Ocker, S. K., & Chatterjee, S. 2022, ApJ, 931, 88
Desvignes, G., Barott, W. C., Cognard, I., Lespagnol, P., & Theureau, G. 2011, in AIP Conf. Ser. 1357, Radio Pulsars: An Astrophysical Key to Unlock the Secrets of the Universe, ed. M. Burgay et al. (Melville, NY: AIP), 349
Dong, Y., Eftekhari, T., Fong, W.-F., et al. 2024, ApJ, 961, 44
Eftekhari, T., & Berger, E. 2017, ApJ, 849, 162
Fabricant, D., Fata, R., Epps, H., et al. 2019, PASP, 131, 075004
Finkelstein, S. L., Ryan, R. E. J., Papovich, C., et al. 2015, ApJ, 810, 71
Flewelling, H. A., Magnier, E. A., Chambers, K. C., et al. 2020, ApJS, 251, 7
Fonseca, E., Andersen, B. C., Bhardwaj, M., et al. 2020, ApJL, 891, L6
Fruchter, A. S., Levan, A. J., Strolger, L., et al. 2006, Natur, 441, 463
Gaia Collaboration, Vallenari, A., Brown, A. G. A., et al. 2023, A&A, 674, A1
Gordon, A. C., Fong, W.-f., Kilpatrick, C. D., et al. 2023, ApJ, 954, 80
Gordon, A. C., Fong, W.-f., Simha, S., et al. 2024, ApJL, 963, L34
Gould, D. M., & Lyne, A. G. 1998, MNRAS, 301, 235
Greisen, E. W. 2003, in Information Handling in Astronomy—Historical Vistas, ed. A. Heck (Dordrecht: Kluwer), 109
Guillemot, L., Cognard, I., van Straten, W., Theureau, G., & Gérard, E. 2023, A&A, 678, A79
Hallinan, G., Ravi, V., Weinreb, S., et al. 2019, BAAS, 51, 255
Harris, W. E. 1996, AJ, 112, 1487
Heintz, K. E., Prochaska, J. X., Simha, S., et al. 2020, ApJ, 903, 152
Hessels, J. W. T., Spitler, L. G., Seymour, A. D., et al. 2019, ApJL, 876, L23
Hewitt, D. M., Bhandari, S., Marcote, B., et al. 2024, MNRAS, 529, 1814
Hewitt, D. M., Hessels, J. W. T., Ould-Boukattine, O. S., et al. 2023, MNRAS, 526, 2039
Hotan, A. W., van Straten, W., & Manchester, R. N. 2004, PASA, 21, 302
Houben, L. J. M., Spitler, L. G., ter Veen, S., et al. 2019, A&A, 623, A42
Hutschenreuter, S., Anderson, C. S., Betti, S., et al. 2022, A&A, 657, A43
Ibik, A. L., Drout, M. R., Gaensler, B. M., et al. 2024, ApJ, 961, 99
James, C. W., Osłowski, S., Flynn, C., et al. 2020, MNRAS, 495, 2416
Johnston, S., & Kerr, M. 2018, MNRAS, 474, 4629
Josephy, A., Chawla, P., Fonseca, E., et al. 2019, ApJL, 882, L18
Kasen, D., & Bildsten, L. 2010, ApJ, 717, 245
Keimpema, A., Kettenis, M. M., Pogrebenko, S. V., et al. 2015, ExA, 39, 259
Kirsten, F., Marcote, B., Nimmo, K., et al. 2022, Natur, 602, 585
Kirsten, F., Snelders, M. P., Jenkins, M., et al. 2021, NatAs, 5, 414
Kremer, K., Piro, A. L., & Li, D. 2021, ApJL, 917, L11
Kumar, A., Maan, Y., & Bhusare, Y. 2024, arXiv:2406.12804
Lanman, A. E., Andersen, B. C., Chawla, P., et al. 2022, ApJ, 927, 59
Lanman, A. E., Andrew, S., Lazda, M., et al. 2024, AJ, 168, 87
Law, C. J., Sharma, K., Ravi, V., et al. 2024, ApJ, 967, 29
Lee-Waddell, K., James, C. W., Ryder, S. D., et al. 2023, PASA, 40, e029
Macquart, J. P., Prochaska, J. X., McQuinn, M., et al. 2020, Natur, 581, 391
Macquart, J. P., Shannon, R. M., Bannister, K. W., et al. 2019, ApJL, 872, L19
Manchester, R. N., Hobbs, G. B., Teoh, A., & Hobbs, M. 2005, AJ, 129, 1993
Marcote, B., Kirsten, F., Hessels, J., et al. 2022, in European VLBI Network Mini-Symp. and Users' Meeting 2021, Vol. 2021 (Trieste: SISSA), 35
Marcote, B., Nimmo, K., Hessels, J. W. T., et al. 2020, Natur, 577, 190
Marcote, B., Paragi, Z., Hessels, J. W. T., et al. 2017, ApJL, 834, L8
Margalit, B., & Metzger, B. D. 2018, ApJL, 868, L4

Marnoch, L., Ryder, S. D., James, C. W., et al. 2023, MNRAS, 525, 994
Martí-Vidal, I., Roy, A., Conway, J., & Zensus, A. J. 2016, A&A, 587, A143
McConnachie, A. W. 2012, AJ, 144, 4
McKinven, R. & CHIME/FRB Collaboration 2022, ATel, 15679, 1
Mckinven, R., Gaensler, B. M., Michilli, D., et al. 2023, ApJ, 951, 82
McMullin, J. P., Waters, B., Schiebel, D., Young, W., & Golap, K. 2007, in ASP Conf. Ser. 376, Astronomical Data Analysis Software and Systems XVI, ed. R. A. Shaw, F. Hill, & D. J. Bell (San Francisco, CA: ASP), 127
Metzger, B. D., Berger, E., & Margalit, B. 2017, ApJ, 841, 14
Nimmo, K., Hessels, J. W. T., Keimpema, A., et al. 2021, NatAs, 5, 594
Nimmo, K., Hessels, J. W. T., Kirsten, F., et al. 2022a, NatAs, 6, 393
Nimmo, K., Hessels, J. W. T., Snelders, M. P., et al. 2023, MNRAS, 520, 2281
Nimmo, K., Hewitt, D. M., Hessels, J. W. T., et al. 2022b, ApJL, 927, L3
Nimmo, K., Pleunis, Z., Beniamini, P., et al. 2024, arXiv:2406.11053
Niu, C. H., Aggarwal, K., Li, D., et al. 2022, Natur, 606, 873
Ocker, S. K., & Cordes, J. M. 2024, RNAAS, 8, 17
Panther, F. H., Anderson, G. E., Bhandari, S., et al. 2023, MNRAS, 519, 2235
Perley, D. A., Fremling, C., Sollerman, J., et al. 2020, ApJ, 904, 35
Petroff, E., Hessels, J. W. T., & Lorimer, D. R. 2022, A&ARv, 30, 2
Planck Collaboration, Aghanim, N., Akrami, Y., et al. 2020, A&A, 641, A6
Prochaska, J. X., Hennawi, J., Cooke, R., et al. 2020a, pypeit/PypeIt: Release v1.0.0, Zenodo, doi:10.5281/zenodo.3743493
Prochaska, J. X., Hennawi, J. F., Westfall, K. B., et al. 2020b, JOSS, 5, 2308
Prochaska, J. X., & Zheng, Y. 2019, MNRAS, 485, 648
Rajwade, K. M., Driessen, L. N., Barr, E. D., et al. 2024, MNRAS, 532, 3881
Ransom, S. M. 2001, PhD thesis, Harvard Univ., Massachusetts
Ravi, V., Catha, M., D'Addario, L., et al. 2019, Natur, 572, 352
Reddy, N. A., & Steidel, C. C. 2009, ApJ, 692, 778
Reina-Campos, M., Trujillo-Gomez, S., Deason, A. J., et al. 2022, MNRAS, 513, 3925
Rickett, B. J. 1990, ARA&A, 28, 561
Sammons, M. W., Deller, A. T., Glowacki, M., et al. 2023, MNRAS, 525, 5653
Savaglio, S., Glazebrook, K., & Le Borgne, D. 2009, ApJ, 691, 182
Schechter, P. 1976, ApJ, 203, 297
Schulze, S., Krühler, T., Leloudas, G., et al. 2018, MNRAS, 473, 1258
Seiradakis, J. H., Gil, J. A., Graham, D. A., et al. 1995, A&AS, 111, 205
Seymour, A., Michilli, D., & Pleunis, Z. 2019, DM_phase: Algorithm for Correcting Dispersion of Radio Signals, Astrophysics Source Code Library, ascl:1910.004
Shannon, R. M., Bannister, K. W., Bera, A., et al. 2024, arXiv:2408.02083
Sharma, K., Ravi, V., Connor, L., et al. 2024, Nature, 635, 61
Shepherd, M. C., Pearson, T. J., & Taylor, G. B. 1994, BAAS, 26, 987
Snelders, M. P., Bhandari, S., Kirsten, F., et al. 2024, ATel, 16542, 1
Sotomayor-Beltran, C., Sobey, C., Hessels, J. W. T., et al. 2013, ionFR: Ionospheric Faraday Rotation, Astrophysics Source Code Library, ascl:1303.022
Spitler, L. G., Scholz, P., Hessels, J. W. T., et al. 2016, Natur, 531, 202
Sridhar, N., & Metzger, B. D. 2022, ApJ, 937, 5
Taggart, K., & Perley, D. A. 2021, MNRAS, 503, 3931
Tendulkar, S. P., Bassa, C. G., Cordes, J. M., et al. 2017, ApJL, 834, L7
Tendulkar, S. P., Gil de Paz, A., Kirichenko, A. Y., et al. 2021, ApJL, 908, L12
Tonry, J. L., Stubbs, C. W., Lykke, K. R., et al. 2012, ApJ, 750, 99
van Bemmel, I. M., Kettenis, M., Small, D., et al. 2022, PASP, 134, 114502
van Dokkum, P. G. 2001, PASP, 113, 1420
van Straten, W. 2004, ApJS, 152, 129
van Straten, W. 2013, ApJS, 204, 13
van Straten, W., & Bailes, M. 2011, PASA, 28, 1
Vanderlinde, K., Liu, A., Gaensler, B., et al. 2019, in Canadian Long Range Plan for Astronomy and Astrophysics White Papers (Meyrin: Zenodo), 28
Virtanen, P., Gommers, R., Oliphant, T. E., et al. 2020, NatMe, 17, 261
Whitney, A. 2004, in European VLBI Network on New Developments in VLBI Science and Technology, ed. R. Bachiller et al. (Madrid: Observatorio Astronomico Nacional of Spain), 251
Whitney, A., Kettenis, M., Phillips, C., & Sekido, M. 2010, in Sixth Int. VLBI Service for Geodesy and Astronomy, ed. D. Behrend & K. D. Baver (Washington, DC: NASA), 192
Willmer, C. N. A., Faber, S. M., Koo, D. C., et al. 2006, ApJ, 647, 853
Wolf, C., Meisenheimer, K., Rix, H. W., et al. 2003, A&A, 401, 73
Xu, H., Niu, J. R., Chen, P., et al. 2022, Natur, 609, 685
Yamasaki, S., & Totani, T. 2020, ApJ, 888, 105
Yang, Y.-P., Li, Q.-C., & Zhang, B. 2020, ApJ, 895, 7